



This is a repository copy of *Characterisation and correlation of areal surface texture with processing parameters and porosity of High Speed Sintered parts*.

White Rose Research Online URL for this paper:
<http://eprints.whiterose.ac.uk/163374/>

Version: Published Version

Article:

Zhu, Z., Lou, S. and Majewski, C. orcid.org/0000-0003-3324-3511 (2020) Characterisation and correlation of areal surface texture with processing parameters and porosity of High Speed Sintered parts. *Additive Manufacturing*, 36. 101402. ISSN 2214-8604

<https://doi.org/10.1016/j.addma.2020.101402>

Reuse

This article is distributed under the terms of the Creative Commons Attribution (CC BY) licence. This licence allows you to distribute, remix, tweak, and build upon the work, even commercially, as long as you credit the authors for the original work. More information and the full terms of the licence here:
<https://creativecommons.org/licenses/>

Takedown

If you consider content in White Rose Research Online to be in breach of UK law, please notify us by emailing eprints@whiterose.ac.uk including the URL of the record and the reason for the withdrawal request.



eprints@whiterose.ac.uk
<https://eprints.whiterose.ac.uk/>



Characterisation and correlation of areal surface texture with processing parameters and porosity of High Speed Sintered parts



Zicheng Zhu^{a,*}, Shan Lou^b, Candice Majewski^a

^a EPSRC MAPP Future Manufacturing Hub, The University of Sheffield, Sheffield, United Kingdom

^b EPSRC Future Metrology Hub, University of Huddersfield, Huddersfield, United Kingdom

ARTICLE INFO

Keywords:

Additive manufacturing
High speed sintering
Areal surface texture
Porosity
X-ray computed tomography
Powder bed fusion

ABSTRACT

High Speed Sintering is an advanced powder bed fusion polymer Additive Manufacturing technique aimed at economical production of end-use parts in series manufacture. Surface finish is thus of high importance to end users. This study investigates the surface topography of High Speed Sintered parts produced using a range of different energy-related process parameters including sinter speed, lamp power and ink grey level. Areal surface texture was measured using Focus Variation microscopy and the sample porosity was systematically examined by the X-ray Computed Tomography technique. Surface topography was further characterised by Scanning Electron Microscopy, following which the samples were subject to tensile testing. Results showed that areal surface texture is strongly correlated with porosity, which can be further linked with mechanical properties. Certain texture parameters i.e. arithmetic mean height S_a , root-mean-square S_q and maximum valley depth S_v were identified as good indicators that can be used to compare porosity and/or mechanical properties between different samples, as well as distinguish up-, down-skins and side surfaces. S_a , S_q and S_v for up- and down-skins were found to correlate with the above energy-related process parameters. It was also revealed that skewness S_{sk} and kurtosis S_{ku} are related to sphere-like protrusions, sub-surface porosity and re-entrant features. Energy input is the fundamental reason that causes varying porosity levels and consequently different surface topographies and mechanical properties, with a 10.07 μm and a 30.21 % difference in S_a and porosity, respectively, between the 'low' and 'high' energy input.

1. Introduction

Additive Manufacturing (AM) has been increasingly used to produce end-use components and products in recent years [1]. Continued technological advances have enabled certain AM processes such as powder bed fusion (PBF) based processes to make significant inroads into a broad market including aerospace, automotive, medical devices and consumer goods [2]. However, one of the main drawbacks that impedes the wide adoption of AM in industry is the surface roughness being at least an order of magnitude higher than other parts manufactured by traditional processes such as machining and injection moulding [3].

Defects on functional surfaces can eventually result in the failure of the component in service [4,5]. Therefore, research has been undertaken to characterise surface topography of AM parts and to understand the influence of AM process parameters on surface roughness [6]. The research reported in the literature can be divided into two major areas, namely PBF metal- and polymer AM-related. In metal AM, Charles et al.

[7,8] assessed the impact of using different laser powers, scan speeds and hatch spacing on the generated surface roughness of the down-facing surfaces of the Selective Laser Melted (SLM) parts. Whip et al. [9] identified a strong correlation between surface average height (S_a), maximum valley depth (S_v) with laser powder in SLM. It was found that S_a and S_v decreased as the laser power increased. Similar findings were also reported by Koutiri et al. [10] and Calignano et al. [11] who also found that the scan speed had the greatest impact amongst laser power and hatch distance. Gockel et al. [4] attempted to correlate S_a and S_v with the fatigue strength of alloy 718 samples produced by SLM. Different laser contour parameters were used to first identify the trend of surface roughness variations, which were then correlated with the fatigue life. Increased S_v was found to correspond with a reduced fatigue life. The effect of build orientation on surface topography has also been researched. Fox et al. [12] reported that surface roughness (R_a) of overhanging features on SLM parts was not correlated with the build orientation. However, Sidambe [13] argued that the horizontal surfaces had a smoothest surface texture whereas the surfaces of the sample

* Corresponding author.

E-mail address: zicheng.zhu@sheffield.ac.uk (Z. Zhu).

<https://doi.org/10.1016/j.addma.2020.101402>

Received 2 January 2020; Received in revised form 4 June 2020; Accepted 15 June 2020

Available online 22 June 2020

2214-8604/ © 2020 The Authors. Published by Elsevier B.V. This is an open access article under the CC BY license (<http://creativecommons.org/licenses/by/4.0/>).

built in the vertical direction were found to be rough, attached with large volume of partially melted powder particles. Tian et al. [14] and Strano et al. [15] also found consistent results. In addition to laser power, scan speed, hatch spacing and build orientation, other process parameters that were studied include weld track width [16] in Electron Beam Melting (EBM) and laser scanning direction [17] in SLM. The research in the polymer AM field adopted approaches similar to metal AM to investigate the effect of process parameters on surface roughness. Mavoori [18] attempted to identify the appropriate laser power, layer thickness and bed temperature for Laser Sintering (LS) of polyamide-12 (PA12) parts. Sachdeva et al. [19] examined the surface roughness variations of PA12 parts fabricated by different laser powers, bed temperatures and hatch spacing in LS. The laser power between 28–32 W, 0.2 mm hatching and 175 °C bed temperatures were found to result in the lowest surface roughness R_a (i.e. 5.46 μm). A similar study was conducted by Negi et al. [20], who identified that hatch spacing was the most significant factor, followed by laser power and scan speed for LS of glass-filled polyamide parts. Van Hooreweder et al. [21] pointed out that the layer-wise production manner and unmolten particles that stuck on the contour of LSed parts were considered to be the main reasons that led to the surface roughness being an order of magnitude higher than that in injection moulding. Strano et al. [22] analysed the effect of build orientation on surface roughness R_a , whereby a computational model was developed to optimise build orientation and energy consumption.

As surfaces of additively manufactured parts are different from those produced by conventional processes, developing specific methods and surface parameters for AM surface characterisation has become a popular topic in recent years [6]. It is noted that, while most of these methods and parameters seem to be generic, the efficacy of these methods was usually demonstrated on metal AM surfaces, as reported in the literature. Pagani et al. [23] proposed a new method for measuring freeform surfaces and re-entrant features. A set of 3D surface texture parameters was defined based on triangular mesh, which was able to represent specific 3D surface topography features such as re-entrant features that cannot be precisely measured by traditional measurement techniques. Du Plessis and le Roux [24] proposed a method to standardise the procedures for measuring surface texture parameter S_a and dimensional accuracy of metal AM parts. Zanini et al. [25] investigated the validity of using a set of generalised surface texture parameters to represent re-entrant features on the SLMed part surfaces. Lou et al. [26] developed a bespoke characterisation procedure for PBF metal surfaces where the robust Gaussian regression and the morphological filters were adopted to separate waviness component in roughness measurements. In the paper by Klingaa et al. [27], a new method for characterising surface texture of internal surfaces of SLMed conformal cooling helical channels was proposed. On the PBF polymer side, Vetterli et al. [28] proposed and evaluated a novel method for characterising surfaces processed via LS. An elastomeric gel pad was pressed onto the surface, enabling the reflective skin on the other side of the pad to form a positive imprint. The pressure depending on the surface topography was detected by a sensor, allowing a height map to be calculated. The results showed a consistent measurement repeatability and reproducibility within 4% and 6% error range, respectively.

In recent years, three-dimensional (3D) areal surface texture measurement has been progressively accepted as an appropriate way to characterise AM surfaces as compared to two-dimensional profile measurement [3]. Tactile and optical methods are the two industrially recognised mainstream techniques for texture measurements [29], and X-ray Computed Tomography (XCT) technique has also drawn significant attention due to the capability to measure hard-to-reach and internal surfaces [3,30–32]. The majority of the effort was made in the PBF metal domain. Thompson et al. [33] conducted a quantitative comparison between optical and XCT techniques for areal surface topography measurements of SLMed parts. Results showed that XCT was the least repeatable. Townsend et al. [34] assessed the validity of using

XCT for surface topography measurements, in terms of measurement deviation, repeatability and reproducibility. Triantaphyllou et al. [35] measured the areal surface texture of SLM and EBM parts using both optical and tactile methods, and claimed that the difference between them was of little significance. Cabanettes et al. [36] further added that the optical Focus Variation technique was well suited for measuring surface texture of SLMed parts built in different orientations. In addition to metal AM work, systematic comparisons between tactile profile and optical measurement techniques were also conducted to characterise surface texture of Laser Sintered polymer parts [29]. Launhardt et al. [29] found that the tactile method resulted in the most repeatable and reproducible results whereas it usually caused minor damages to the measured surfaces. By contrast, optical methods showed unique advantages in characterising and visualising 3D surface topography, with Focus Variation being the most reliable amongst other optical methods.

High Speed Sintering (HSS), as a novel and disruptive PBF based AM technique, was invented specifically for medium to high volume production of end-use components [37,38]. The surface quality is therefore of high importance to end users. Areal surface texture measurement is increasingly gaining consensus as the current best way of characterising the 3D surface topography of an additively manufactured part [3]. However, the eventual surface topography is affected by a number of factors involved in the sintering process including energy source, feedstock material, fusion of powder particles etc. Thus, this study aims to understand this complex interaction between surface texture and the HSS energy-related process parameters through investigating areal surface texture, porosity and the resulting mechanical properties. Three process parameters (sinter speed, lamp power and ink grey level) were studied. The experimental methods are described in Section 2. The results are presented in Section 3, which is followed by in-depth discussion and conclusions in Sections 4 and 5.

2. Material and methods

2.1. Material

Virgin PA2200 (polyamide-12, also known as Nylon-12) supplied by EOS GmbH was used as the raw material powder to manufacture the test samples. This is the most ‘standard’ and repeatable material for powder bed polymer AM [39], and is the most well-documented material to date for HSS. The average powder size was 56 μm and D90 was 90 μm .

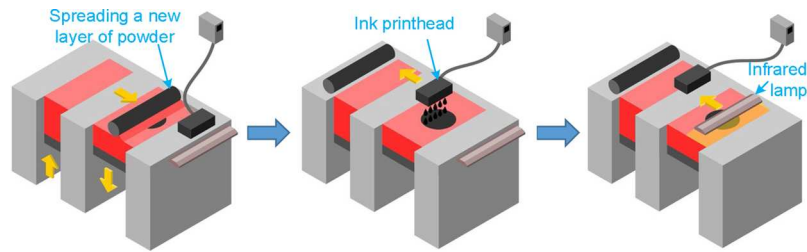
2.2. The High Speed Sintering process and machine

HSS, as shown in Fig. 1a, uses an infrared lamp as a thermal energy source to melt a selectively-applied radiation absorbing ink, causing the underlying powder particles to sinter and coalesce [38]. The ink is first jetted from the inkjet printhead onto a fresh layer of pre-heated powder, as shown in Fig. 1b. The entire powder bed is then exposed to infrared radiation using the infrared lamp, which causes the ink to rapidly absorb sufficient energy to sinter the underlying powder particles [40]. Areas without ink remains unsintered. This is followed by re-coating a new layer of powder, and the process continues until the object is built. The HSS system used in this study was a Voxeljet VX200, which has a maximum build size of 300 × 200 × 150 mm³.

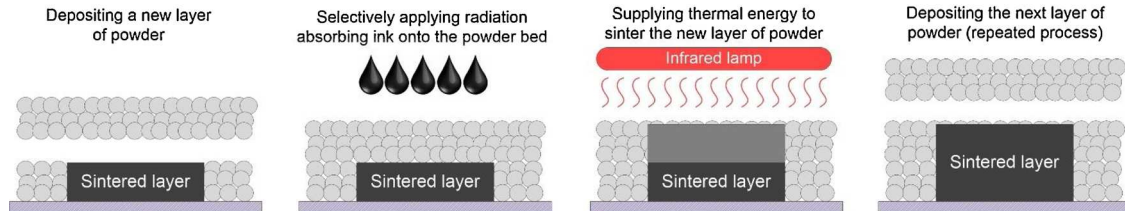
2.3. Design of experiments

2.3.1. HSS process parameters

From the literature review presented in Section 1, surface topography is the result of a series of complex interactions involved in the sintering process. Given that the sintering of powder particles are largely determined by the thermal energy that is input into the part on the powder bed, three thermal energy-related process parameters were



(a) Schematic of the High Speed Sintering process



(b) Detailed view of the Sintering process, adapted from [41]

Fig. 1. The High Speed Sintering process [41].

investigated in this study, which were sinter speed, infrared lamp power and ink grey level.

- **Sinter speed** – the speed at which the lamp passes over the bed. The lower the sinter speed, the higher thermal energy that is input into the powder bed per unit time.
- **Lamp power** – the power at which the lamp radiates infrared. With a constant sinter speed, changing the power of the infrared lamp can effectively result in increased and decreased energy input to the powder bed.
- **Ink grey level** – the amount of ink to be jetted onto the powder bed. The ink will absorb heat from the lamp radiation, causing powder particles to sinter. A higher ink grey level means a greater amount of ink to be dispensed.

It is noted that the ink, supplied by Sun Chemical Corp [42], contains carbon black in petroleum distillates. Carbon black is a strong infrared absorber, and a typical particle size is approximately 100 nm. The parameter ‘ink grey level’ (a dimensionless parameter) that is widely used in the inkjet industry describes the degree of coverage of the desired area by ink, which is determined by the volume of the droplet ejected from the printhead [37]. The printhead installed in the Voxeljet VX200 system is a native 360 nozzle per inch (npi) inkjet printhead provided by Xaar® 3D Ltd. [43]. The volume per drop is six picolitres (pL) and the grey levels are also set at linear increments of six pL per dot. Grey level 1 means one drop per dot at 360 npi, and grey level 2 represents two drops per dot at 360 npi. Therefore, grey levels 1, 2, 3 and 4 can be quantitatively expressed as ink deposition (pL/mm²) of 1205.28, 2410.56, 3615.84 and 4821.12 pL/mm², respectively, according to Eq. 1 below.

$$\text{ink deposition (pL/mm}^2\text{)} = \left(\frac{360}{25.4}\right)^2 \times \text{grey level} \times 6 \quad (1)$$

Other parameters that were kept constant included the layer thickness of 0.1 mm, powder bed pre-heat temperature of 160 °C, 45 min pre-heat time prior to printing, and 60 min cooling time after printing. The samples were then post-processed in a bead blasting machine to remove surrounding powders.

2.3.2. The Taguchi experimental design

The experiments were designed with two objectives in mind:

- To systematically examine the effect of the above three process parameters on the resulting surface topography.
- To investigate the relationships between the surface topography with porosity and mechanical properties of the produced samples, namely, whether mechanical properties are influenced by specific surface topographic characteristics.

The Taguchi Design of Experiments L9 array was thus employed and the three-level variables are defined in the following Table 1. Please note, although energy density calculation methods exist for some PBF processes [44–47], none currently exist for HSS. Energy input variations have therefore been assessed through use of combinations of a low, medium and high value of each parameter, as listed in Table 1. The parameter sets chosen are within the most reliable process window for HSS, and based on recommendations from the HSS system manufacturer, i.e. sinter speed of 80–120 mm/s, lamp power of 750–1000 W and ink grey level of 2–4.

2.3.3. Building process layout and test samples

Fig. 2 shows the layout of the build. In each set of samples, there were five ASTM D638 Type I tensile bars [48] and two cuboids of 8 ×

Table 1

The Taguchi L9 array for the investigation of areal surface texture in relation to HSS process parameters and porosity.

Set number	Energy-related parameter		
	Sinter speed (mm/s)	Lamp power (W)	Ink Grey level
1	80	750	2
2	80	875	3
3	80	1000	4
4	100	750	3
5	100	875	4
6	100	1000	2
7	120	750	4
8	120	875	2
9	120	1000	3

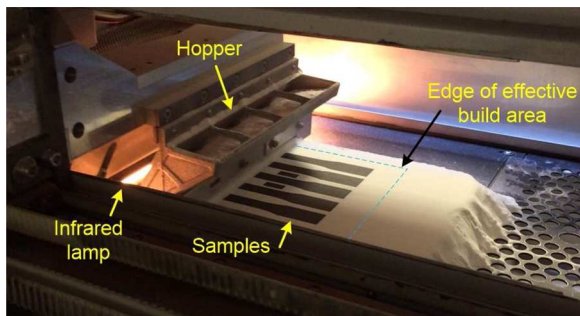


Fig. 2. The layout of the building process on the HSS system.

$20 \times 3.2 \text{ mm}^3$ (XYZ). Samples were arranged at 5 mm spacing at least in order to minimise thermal interaction between neighbouring parts. All samples were at least 15 mm distance from the edge of the effective build area. Nine sets of samples were produced, in accordance with the Taguchi L9 array shown in Table 1. A set of produced samples is shown in Fig. 3.

Cuboids were used for surface topography characterisation. It is noted that there are other artefacts discussed in the literature [3,9,33,49] that have been proposed for measurements of AM surfaces, mainly for metal AM. Given that the cuboids will also be subject to XCT scans for porosity measurements and more importantly this study is aimed at exploring the effect of HSS process parameters on the variation of surface topography, the authors decided to use the above shape and dimensions. To reduce uncertainties e.g. noise and beam hardening in XCT scans, two cuboids in each set were scanned and the porosity levels were compared. For tensile testing, the five tensile bars in each set were used.

2.4. Measurements, characterisation and testing

The five activities presented below were undertaken in sequence to acquire quantitative and qualitative information on surface topography, porosity and mechanical properties.

2.4.1. Areal surface texture measurements

Areal surface topography was measured using a structured light Alicona InfiniteFocusSL [50] laser profilometer, which is Focus Variation (FV) microscopy that scans an area of interest in 3D. ISO 25178–2 [51] defines terms, definitions and areal parameters for surface texture characterisation. In general, areal parameters have distinct advantages compared with profile parameters e.g. arithmetic mean deviation of the profile R_a in ISO 4287 [52]. This is because surface topography is three-dimensional whereas profile parameters measured in 2D are unable to provide a complete description of the real surface [3]. The areal surface texture parameters chosen were S_a , S_q , S_v , S_{ku} and S_{sk} . The description of these parameters are provided in Table 2. S_a and S_q are the most common texture parameters [6]. S_v was chosen as it was reported to have a potential impact on crack initiation causing reduced mechanical properties [4]. S_{ku} and S_{sk} are recommended for AM surface characterisation [3].

A total of five measurements at different positions were taken per surface (i.e. up-skin, down-skin* and side surface) per sample. In each measurement, an area of $2.0 \times 2.0 \text{ mm}^2$ was scanned and the data was processed in Alicona MeasureSuite 5.3. It is noted that there have not been established international standards on the size of the measured area specifically for AM surface metrology. In general, measuring lengths and cut-off wavelengths for a sequence of R_a ranges are specified in ISO 4288 [53], which is applied to areal measurement per ISO



Fig. 3. A set of test samples produced by the HSS process.

Table 2

Areal surface texture parameters measured in this study.

Parameter	Description
S_a	Arithmetic mean height of selected area
S_q	Root-Mean-Square height of selected area
S_v	Maximum valley depth of selected area
S_{sk}	Skewness of selected area. It describes how the mass is distributed around the mean plane.
S_{ku}	Kurtosis of selected area. It is a measure of the sharpness of the surface roughness over the area.

25178–3 [54]. Based on the above, the measuring length of 8 mm for AM surface measurements was proposed by Townsend et al. [3] and Triantaphyllou et al. [35]. However, there have been some concerns and discussions as it is a rather large area for optical surface measurements compared with traditional tactile profilometry. In addition, due to AM parts being intrinsically small and complex, some AM surfaces are smaller than $8 \times 8 \text{ mm}^2$. There is thus no conformance on AM measurement area and there are debates that current ISO standards, which were originally designed for machined surfaces, cannot directly be applied to AM surfaces without amendments. It is also noted that other lengths/sizes were also adopted in different studies reported in the literature (e.g. $2.9 \times 2.9 \text{ mm}^2$ by Thompson et al. [33], $1.4 \times 1.89 \text{ mm}^2$ by Whip et al. [9], $1.62 \times 1.62 \text{ mm}^2$ by Newton et al. [55], $2.5 \times 3.0 \text{ mm}^2$ by Koutiri et al. [10], 4 mm long linear measurements by Brika et al. [56] and $5 \times 3 \text{ mm}^2$ by Khorasani et al. [57]). Hence, in this study, an area of $2.0 \times 2.0 \text{ mm}^2$ was scanned in each measurement, and five measurements in total were performed at different regions across the surface area, following which the average was used to present the surface topography.

2.4.2. X-ray computed tomography scans for porosity measurements

The cuboids were scanned using Nikon Metrology 225/320 kV Custom Bay system. An accelerating voltage of 100 kV, power of 17.6 V and 500 ms exposure were used in the scans. The achieved voxel size was $10.0 \mu\text{m}$. 3D data was reconstructed from the 2D radiographs using a filtered back projection algorithm. The data was then analysed using FEI Avizo 9 software with segmentation by the Otsu method [58] to characterise porosity. Porosity in terms of pore volume fraction was calculated using a low pore size cut-off of $2 \times 2 \times 2$ (8) voxels, which was in line with the related research work reported in the literature

* Up-skin refers to the top surface of the sample along the build direction. Down-skin is the bottom surface of the sample.

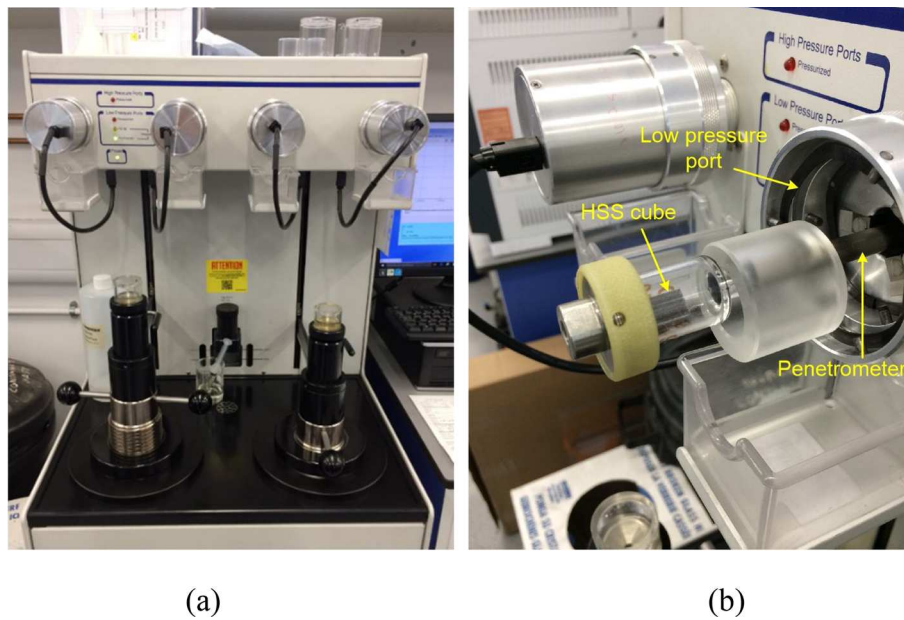


Fig. 4. Mercury intrusion porosimetry: (a) the Micromeritics® AutoPore V system and (b) placing an HSS sample into the low pressure chamber.

[59–61]. The porosity levels of the two cuboids in each set were compared for initial validation.

2.4.3. Scanning electron microscopy (SEM)

Up-, down-skins and side surfaces of each cuboid were examined in SEM to acquire additional qualitative information on surface texture. The cuboids were gold coated in vacuum, and SEM was performed on a Tescan Vega3 system in 10 kV, with a maximum magnification of 3000x.

2.4.4. Tensile testing

Tensile tests were performed on Tinius Olsen tensile machine to quantify the Ultimate Tensile Strength (UTS) and Elongation at Break (EAB) of the test specimens. The test speed was 5 mm/min. Where possible, ASTM D638 Standards [48] were followed during testing.

2.4.5. Mercury intrusion porosimetry measurements for porosity validation

In order to cross-evaluate the results of porosity measurements obtained by XCT, additional mercury intrusion porosimetry (MIP) was conducted on a Micromeritics® AutoPore V system, as shown in Fig. 4a. In each measurement, a cube was held in a section of the penetrometer cell shown in Fig. 4b. The cube was subject to low and high pressure tests in sequence, with a starting pressure of 30.00 psia, pressure increments from 10.00–2500.00 psia at different stages, an ending pressure of 6.00×10^4 psia, advancing and receding mercury contact angle of 130° , and the equilibrium time of 10 s.

3. Results

This section presents the variations of areal surface texture parameters in relation to porosity levels, mechanical properties and the HSS process parameters i.e. sinter speed, lamp power and ink grey level.

3.1. Relationships of surface texture and porosity

3.1.1. Arithmetic mean and root mean square heights (S_a and S_q)

The variations of arithmetic mean height (S_a) for up-, down-skins and side surfaces in relation to porosity is shown in Fig. 5. The X-axis shows nine sets of samples across all the experiments, and the yellow bar attached to each set shows the porosity level, of which the value can be read on the primary Y-axis on the left. The points in each set are the

corresponding S_a values, which can be read on the secondary Y-axis on the right. The error bars represent the standard deviation across the five measurements. For up- and down-skins, S_a was found to be strongly correlated with porosity. S_a decreased as the porosity reduced, and vice versa. S_a for side surface can also be linked with porosity, and the slight inconsistency (i.e. set 9) was likely due to the limitation of the FV measurement technique incapable of measuring re-entrant features which are rather common on side surfaces (please refer to Section 4.3.1 and Fig. 22). It was also found that down-skin surfaces are the smoothest and side surfaces are the roughest. Root mean square height (S_q) in relation to the porosity level shown in Fig. 6 was found to follow the same pattern as S_a . Table 3 provides some examples of surface topographies of up-skins and the porosities (measured by XCT and MIP techniques) of the nine sets of samples.

3.1.2. Maximum valley depth (S_v)

The graph in Fig. 7 shows the variation of the depth of the deepest valley S_v in relation to porosity. S_v was reported to be a metric that is related to mechanical properties [4] as a deep valley could potentially cause stress concentration acting similarly as a notch. For both up- and down-skins, S_v varied in accordance with porosity levels, exhibiting a strong correlation. A close relationship between S_v of side surfaces and porosity was also observed in most cases except sets 8 and 9. It is also noted that S_v is significantly higher compared with S_a , by up to six times higher. Again, down-skin S_v is in the lowest level and side surface is in the highest level. In addition, there is a large extent of scatter in S_v indicated by the standard deviation, particularly for samples with a high level of porosity (e.g. sets 1, 4, 7 & 8), suggesting a high degree of variability on the surface.

3.1.3. Skewness and kurtosis (S_{sk} and S_{ku})

Skewness (S_{sk}) and kurtosis (S_{ku}) are parameters describing the distribution of the heights/depths of peaks and valleys. They are typically considered to be discriminating parameters to differentiate up- and down-skins if the sample is built at an inclined angle to the powder bed [13,35]. In this study, all samples were built horizontally and thus Figs. 8 and 9 examine the variation of up- and down-skin S_{sk} and S_{ku} in response to porosity. Please note that S_{sk} and S_{ku} for side surface are excluded due to the presence of re-entrant features making S_{sk} and S_{ku} values invalid to a certain extent, which will be discussed in Sections 4.3.1 and 4.4.

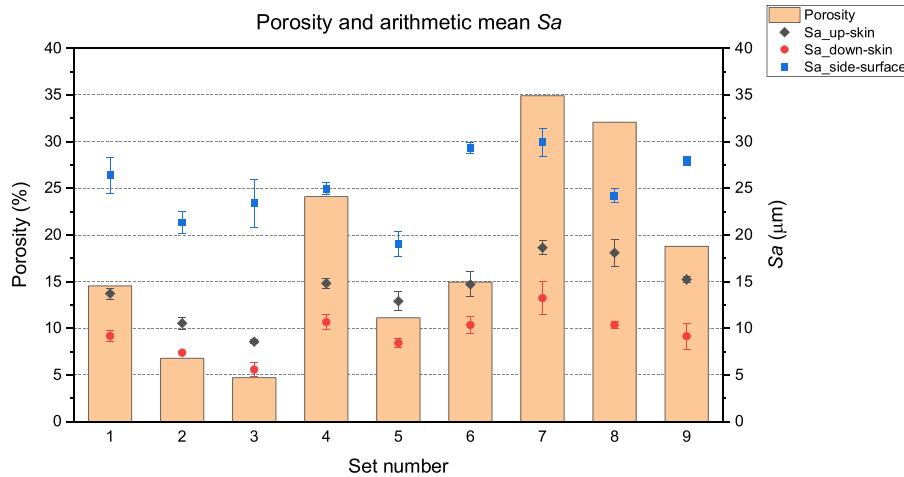


Fig. 5. Relation of Sa to porosity level.

Ssk describes the symmetry of peaks and valleys around the mean plane. If $Ssk = 0$, it means peaks and valleys are evenly distributed around the mean plane. If $Ssk < 0$, the surface is predominated by valleys. By contrast, the surface is dominated by peaks if $Ssk > 0$.

No clear pattern relating to *Ssk* and porosity was found in Fig. 8. By comparing up- and down-skins, down-skin *Ssk* is always higher than up-skin *Ssk*. Therefore, *Ssk* can potentially be used to as an indicator to discriminate up- and down-skins. Additionally, for down-skins, over half of the samples has a positive *Ssk* (i.e. sets 2, 3, 4, 6 & 9), meaning that there are greater number of peaks than valleys. Whereas, most of the up-skins (except set 3) have a negative *Ssk* value, indicating valleys dominate the surface. Negative *Ssk* is likely caused by the presence of open pores and are related to sub-surface porosity (please see Fig. 15, and Sections 4.3 and 4.4).

Kurtosis *Sk_u* is a measure of the expansion and distribution of heights, namely, the sharpness of a surface. In general, $Sk_u = 3$ is the nominal cut-off value, which represents the surface having an equal distribution of soft and sharp peaks and valleys. If $Sk_u < 3$, the surface is considered to primarily consist of squashed peaks and valleys with a relatively large edge radius, which, for AM surfaces, can be interpreted as less likely to initiate cracks under loads as compared to spiked peaks and valleys. On the other hand, if $Sk_u > 3$, the surface is characterised by sharp peaks and valleys with a relatively small edge radius.

Sk_u for both up- and down-skins is greater than 3 as shown in Fig. 9, indicating that the majority of peaks and valleys is sharp. For samples with a low level of porosity (i.e. sets 2 and 3 with a porosity of 6.79 % and 4.71 %, respectively), up- and down-skins have similar *Sk_u* values.

However, there is a significant difference in *Sk_u* for samples that are of high porosity. This is likely due to sub-surface porosities of up- and down-skins being different. For instance, in sets 5 and 6, it appears that the bottom layers of the sample is significantly less porous than the top layers (shown in Table 3), resulting in a large discrepancy in up- and down-skins *Sk_u* values. Further discussion can be found in Section 4.4.

3.2. Relationships between surface texture and HSS process parameters

The varying HSS process parameters with the associated surface texture of up-, down-skins and side surfaces are plotted in Figs. 10–13.

3.2.1. Arithmetic mean and root mean square heights (Sa and Sq) in relation to process parameters

Sa for all up-skin, down-skin and side surfaces increased as the sinter speed increased, shown in Fig. 10. In particular, *Sa* for the up-skin showed a significant trend with the sinter speed with a *P*-value lower than 0.05. An inverse trend was found for the ink grey level. *Sa* for all up-, down-skins and side surfaces increased with a decrease in ink grey level, indicating an improved surface roughness. Increasing lamp powers also led to a decreased *Sa* for both up- and down-skins, but using a high power might potentially be detrimental to the side surface *Sa*, as shown in Fig. 10c. Having said that, it is well known that side surfaces of AM parts have re-entrant features [25,35] that result in measurement inaccuracies potentially in a large extent in FV measurements. This will be further discussed in Section 4.3.1. The *P*-values for down-skin and side surface *Sa* suggest that they are more susceptible

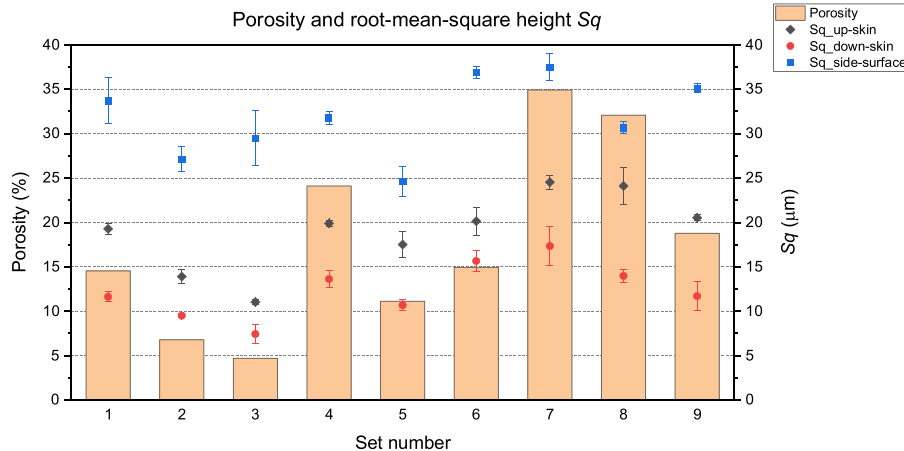


Fig. 6. Relation of Sq to porosity level.

Table 3

Surface topographies of up-skins and porosities. The XCT images show the front view of a projection slice, and the build direction is from bottom to top.

Set number	Height map	Porosity tomography image
Set 1 $S_a = 13.71 \mu\text{m}$ Porosity = 14.54% (measured by XCT), 14.77% (measured by MIP)		
Set 2 $S_a = 10.54 \mu\text{m}$ Porosity = 6.79% (XCT), 6.94% (MIP)		
Set 3 $S_a = 8.56 \mu\text{m}$ Porosity = 4.71% (XCT), 4.55% (MIP)		
Set 4 $S_a = 14.62 \mu\text{m}$ Porosity = 24.11% (XCT), 24.68% (MIP)		
Set 5 $S_a = 12.90 \mu\text{m}$ Porosity = 11.13 % (XCT), 10.96 % (MIP)		
Set 6 $S_a = 16.00 \mu\text{m}$ Porosity = 14.95% (XCT), 15.27% (MIP)		
Set 7 $S_a = 18.63 \mu\text{m}$ Porosity = 34.92% (XCT), 34.49% (MIP)		

(continued on next page)

Table 3 (continued)

Set number	Height map	Porosity tomography image
Set 8 Sa = 18.08 μm Porosity = 32.08% (XCT), 32.36% (MIP)		
Set 9 Sa = 15.24 μm Porosity = 18.78% (XCT), 19.01% (MIP)		

to ink grey level compared with up-skin. Additionally, S_q , which is the root mean square height, was found to be in a trend consistent with the above.

In general, a greater amount of energy input can be obtained, as introduced in Section 2.3.1, by reducing sinter speed, increasing lamp power and/or ink grey level. The trend of S_a/S_q variation in Fig. 10 reveals that increasing energy input can result in a smoother surface. Section 4.2.1 provides an in-depth discussion on the effect of energy input on surface topography.

3.2.2. Maximum valley depth (S_v) in relation to process parameters

Fig. 11 shows the variations of S_v in relation to sinter speed, lamp power and ink grey level. S_v shows a clear trend of increasing S_v with the increased sinter speed, reduced lamp power and ink grey level in most cases. As using a higher speed, a lower power and a lower grey level essentially indicate a lower energy input, S_v can be linked with the degree of powder fusion, which will be discussed in detail in Section 4.2.1.

3.2.3. Skewness and kurtosis (S_{sk} and S_{ku}) in relation to process parameters

Results in Fig. 12 showed that S_{sk} is of a negative value for up-skin, indicating that the up-skin primarily consists of valleys rather than

peaks, which is likely due to the presence of open pores (please see Fig. 15b and c). For down-skins, S_{sk} varies between approximately 0.5 and -0.5 depending on the process parameters used. Using a sinter speed of 100 mm/s, together with 875 W lamp power and ink grey level of 4 resulted in peaks and valleys being evenly distributed around the mean plane for down-skin.

With respect to S_{ku} , the trend for up-skin is that it decreased along with an increase in sinter speed, lamp power and ink grey level, as shown in Fig. 13. The decreased S_{ku} towards the nominal value of 3 indicates a reduced randomness of the surface heights. As for down-skin S_{ku} , it also reduced towards the nominal value of 3 as the lamp power increased. This suggested that peaks and valleys on the down-skins became less sharp when using a higher lamp power. More discussion is given in Sections 4.2.1 and 4.4.

3.3. Porosity and mechanical properties

Tensile testing was performed according to Section 2.4.4 to determine the mechanical properties of the samples. The results presented in Fig. 14 revealed that both UTS and EAB are strongly correlated with the level of porosity. Reduced porosity resulted in an increase in UTS and EAB. The porosity for set 3 is 4.71 %, which is the lowest amongst other sets of builds, resulting in the UTS being the highest. In contrast,

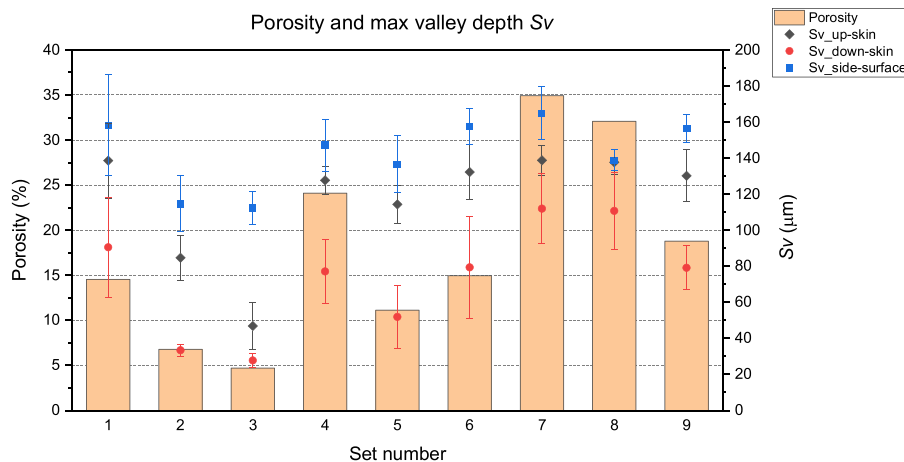


Fig. 7. Variation of S_v in relation to porosity.

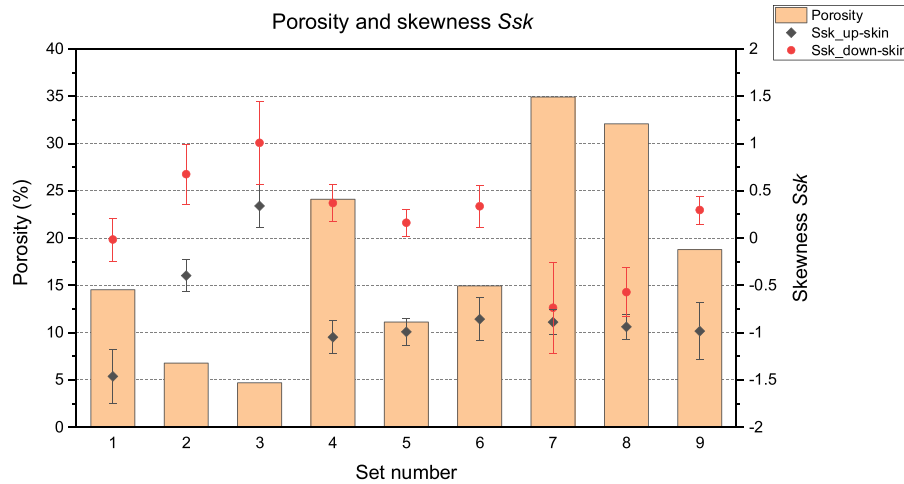


Fig. 8. Skewness Ssk and porosity.

increased porosity, which means the sample was of a lower density with enlarged voids within the material, led to the reduced UTS and EAB. Both UTS and EAB are in the lowest level in set 7 where the porosity is the highest. Given that surface texture (e.g. S_a , S_q and S_v) is closely correlated with porosity, and porosity is strongly correlated with the resultant mechanical properties, a link can be established between surface texture and mechanical properties, which will be presented in Sections 4.1, 4.2 and 4.5.

4. Discussion

4.1. Correlation of areal surface texture with porosity and mechanical properties

Upon analysing the results presented in Section 3, the correlation between areal surface texture, porosity and mechanical properties can be derived as follows, and the reasons behind the correlation are discussed in the proceeding subsections.

- S_a and S_q strongly correlate with porosity (Figs. 5 and 6) and hence, measuring S_a and/or S_q will provide an indication of the porosity level.
- Since porosity is closely correlated with mechanical properties (Fig. 14), areal surface texture can be further linked with mechanical properties, in particular S_a and S_q .
- A general trend for S_a , S_q and S_v is that they increased as the sinter

speed increased, lamp power and ink grey level reduced (Figs. 10 and 11). This means surface roughness increased as the amount of input energy reduced, and vice versa.

- S_{sk} increased as the lamp power increased (Fig. 12), indicating that the surface was less dominated by valleys, primarily due to reduced number of open pores on the surface.
- S_{ku} decreased towards the nominal cut-off value of 3 as the lamp power increased (Fig. 13), suggesting that peaks and valleys were less sharp, in other words, surface became relatively smoother.

4.2. Effect of energy input on surface topography

4.2.1. Fusion of powder particles

One of the most critical underlying reasons that causes the varying surface topographies is the amount of thermal energy involved in the sintering process. It is understandable that using a slow sinter speed and a high lamp power will effectively introduce an increased amount of energy into the build. Fig. 10 demonstrates that S_a reduced as the sinter speed decreased and lamp power increased, indicating an improved surface roughness for up- and down-skins. Increasing the ink grey level resulted in a greater amount of ink jetted onto the part, which enhanced the absorption of heat radiation of the lamp, leading to a smoother surface S_a , shown in Fig. 10. Combinations of sinter speed, lamp power and ink grey level are most likely to have a greater impact on surface texture (i.e. a lower P -value) but this requires further experiments to be carried out.

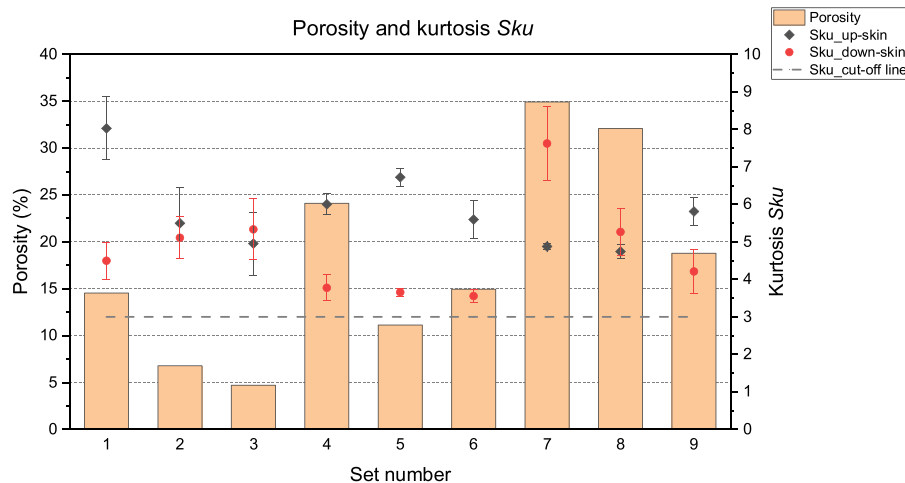


Fig. 9. Kurtosis Sku and porosity.

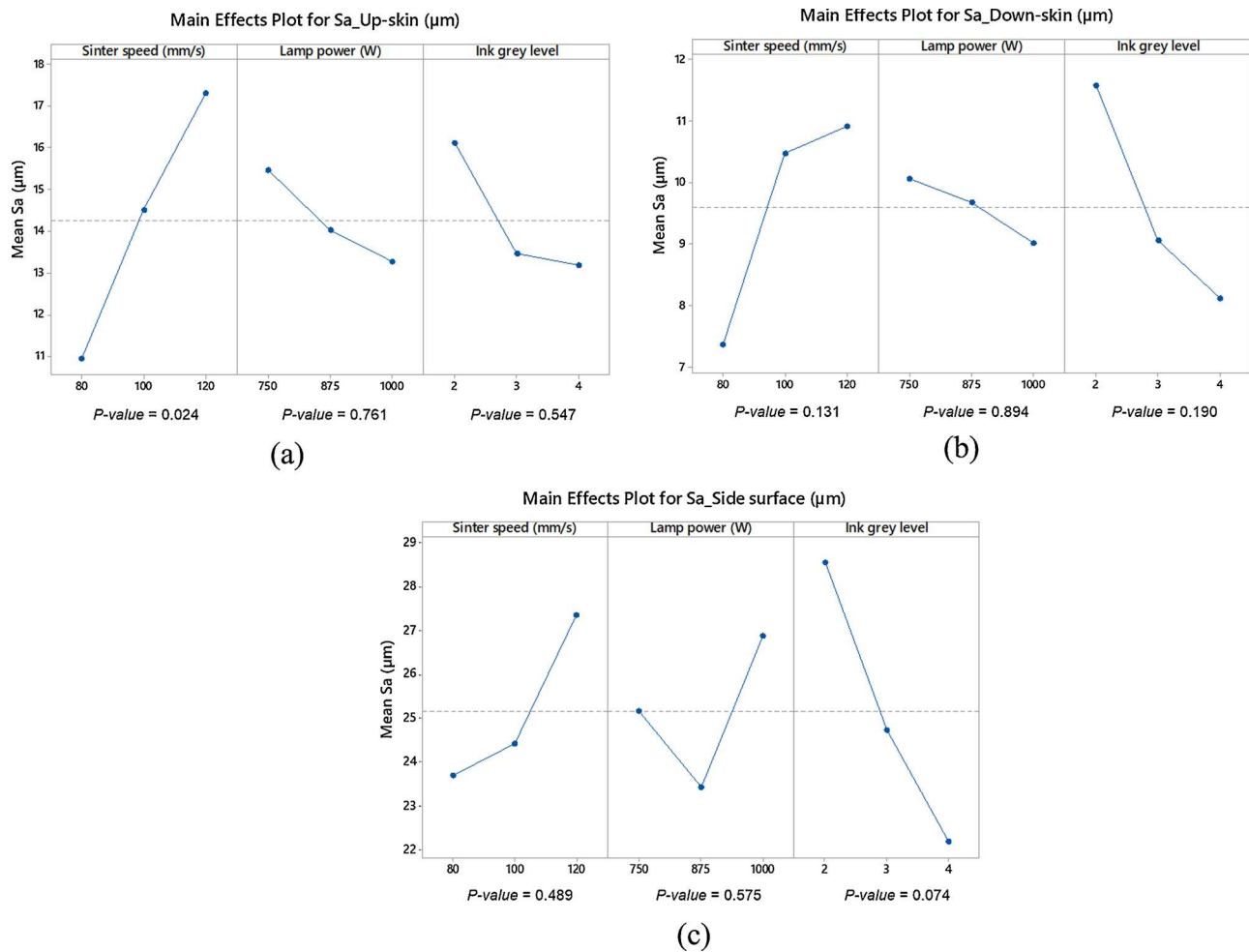


Fig. 10. Main effects plots for surface arithmetic mean (S_a) in relation to the HSS process parameters.

It has been reported by other researchers that energy input is critical to porosity [46,59]. A higher degree of sintering can be obtained with higher lamp powers resulting in formation of parts with enhanced mechanical strength. A higher degree of sintering also leads to parts with a higher density. A greater amount of energy input (to a certain level) on the top layer of powder particles can cause a more uniform and flat surface, and thus a better surface finish [38]. Therefore, areal surface texture is closely related to energy input that has a direct effect on porosity and mechanical properties. This is further evidenced by examining SEM micrographs of the up-skins of the samples in sets 3, 5 and 7 with varying porosity levels of 4.71 %, 11.13 % and 34.92 % in Fig. 15 a, b and c, respectively. The relationship between process parameters, porosity and mechanical properties is elaborated from the aspect of thermal behaviour of the HSS process in the succeeding paragraphs in this section.

Thermal behaviour in HSS usually involves highly sophisticated multi-physics and non-equilibrium thermal phenomena that are driven by a number of parameters including lamp power, sinter speed, ink grey level, layer thicknesses, powder bed temperature and powder physical properties etc. [62]. The thermal energy from the lamp causes powder particles to fuse and consolidate, as illustrated in Fig. 16a. In general, the shell of the powder melts, causing the molten polymer to form necks between neighbouring particles. The difference between the average pressure on the contact area and the surface tension along the peripheries of the two adjacent particles induces a sintering force, which is the thermodynamic force that drives neck growth and shrinkage [63,64]. In addition to the powders that are being melted, the heat also dissipates downwards and outwards primarily via conduction to the previous

layers and surrounding powders [65].

A higher amount of energy input can be achieved by reducing sinter speed, increasing lamp power and/or ink grey level. This tends to favour re-melting of previous layers and provoke a smoothing effect, improving particle fusion and reducing porosity as well as enhancing bonding between particles [9,10]. In HSS, a low viscosity melt is of high importance to HSS because there is no additional compacting force in the HSS process. Unlike injection moulding where a holding pressure is applied during part formation resulting in high density and superior surface quality, HSS relies on melted particles themselves to flow and consolidate, as shown in Fig. 16a. When a high input energy is applied, large particles can be melted more completely, resulting in a lower viscosity melt [70,71]. The lower viscosity melt results in the increased flowability, which increases the tendency of melted particles to flow outwards, creating a smoother surface. Therefore, it was observed in Figs. 10 and 11 that the surface roughness S_a and maximum valley depth S_v of both up- and down-skins decreased as the lamp power and ink deposition increased, and sinter speed reduced. As the HSS process continued, the heat generated in the next layer transmitted to the previous layer, causing continued heat accumulation. The accumulated heat had certain effect on reducing the cooling rate, in which case long molecule chains had more time to rearrange, resulting in the increased degree of crystallinity [70,72]. A higher degree of crystallinity usually indicates a lower molecular chain activity and porosity. The reduced porosity in the bottom half of the specimens in sets 5 and 6 in Table 3 also confirms the effect of heat accumulation. Moreover, given that the lamp irradiates the entire powder bed as it traverses (shown in Fig. 2), increasing lamp power or decreasing sinter speed will rise the

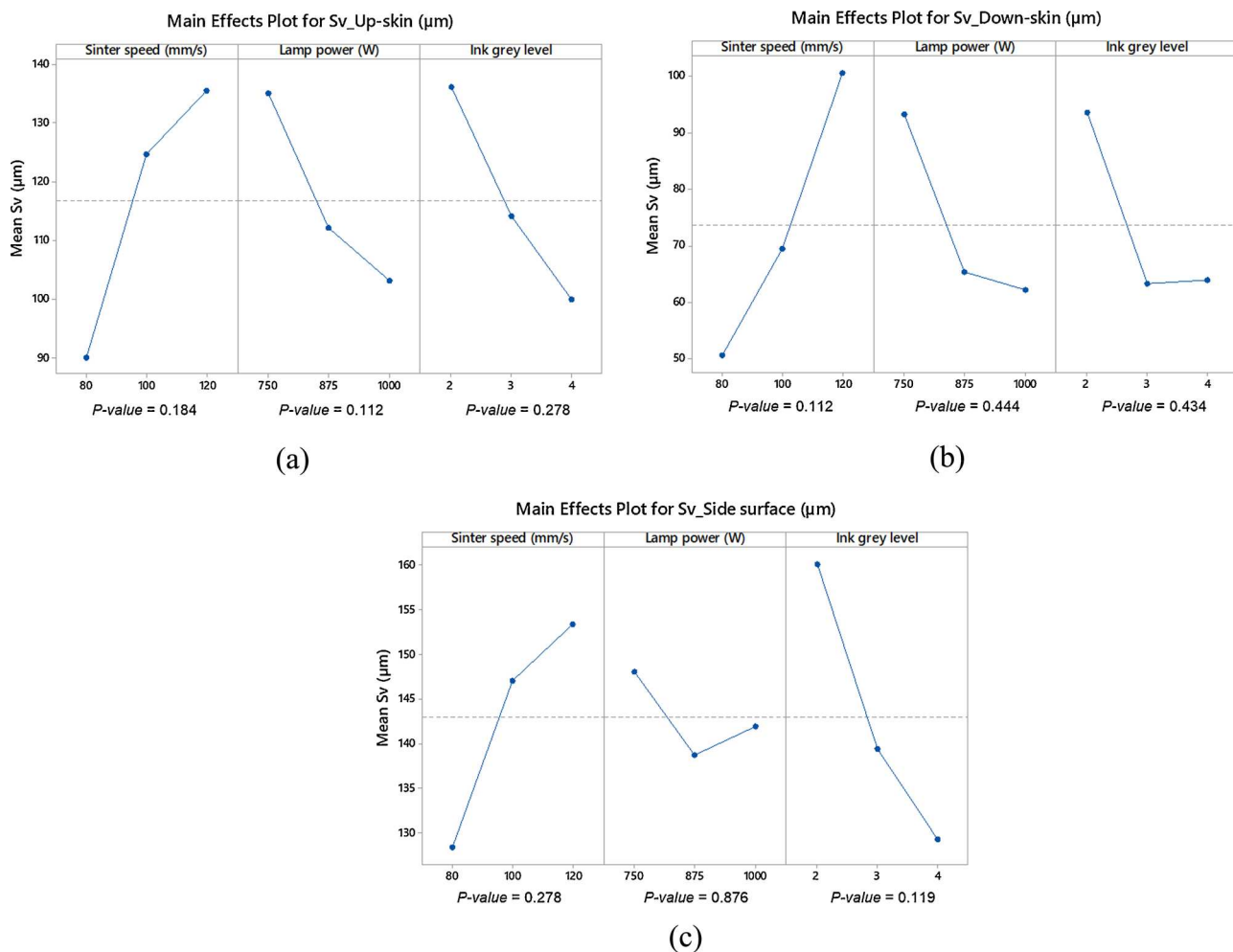


Fig. 11. Main effects plots for maximum valley depth (*Sv*) in relation to the HSS process parameters.

temperature of the entire powder bed, which accelerates heat accumulation effect, causing a lower viscosity melt and as a result, a smoother surface [73].

On the other hand, insufficient energy input, caused by reducing lamp powers, increasing sinter speed or decreasing amount of ink deposition, results in a decreased powder temperature as well as a diminished phenomenon of remelting of previous layers. Consequently, this causes a reduced degree of heat accumulation and crystallinity, and

a relatively high viscosity melt, which eventually increases surface roughness and porosity. Incomplete fusion, as depicted in Fig. 16b, leaves voids between particles, resulting in increased surface roughness. The highly porous structure throughout the entire specimens in sets 7 and 8 shown in Table 3 demonstrates the lack of heat accumulation and incomplete fusion. Partially sintered particles and voids as a result of this lack of fusion can be clearly seen in Fig. 15c, which negatively affected surface quality. Moreover, an example of the comparison of the

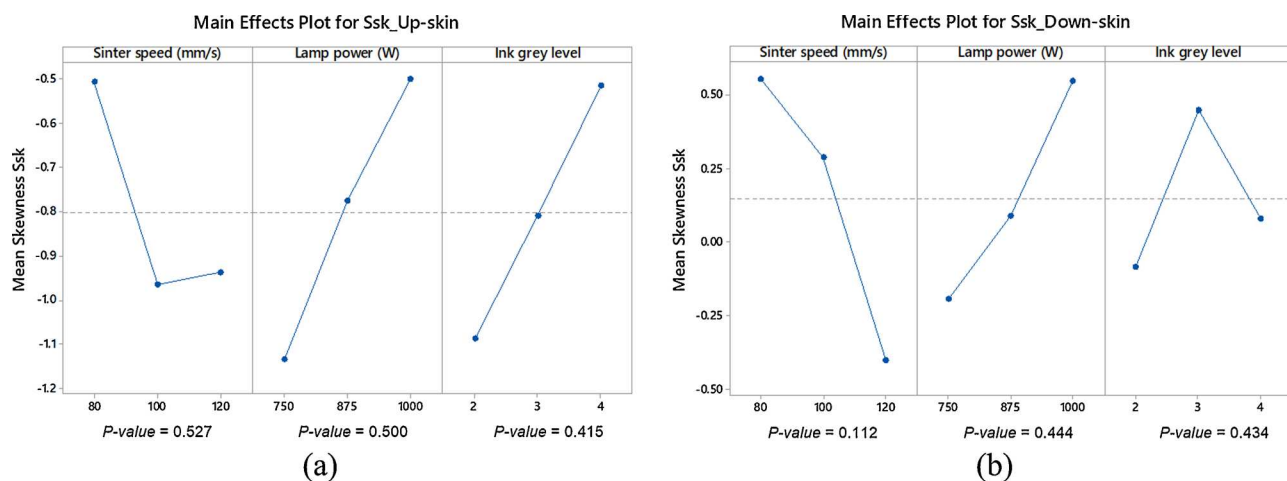


Fig. 12. Main effects plots for skewness (*Ssk*) in relation to the HSS process parameters.

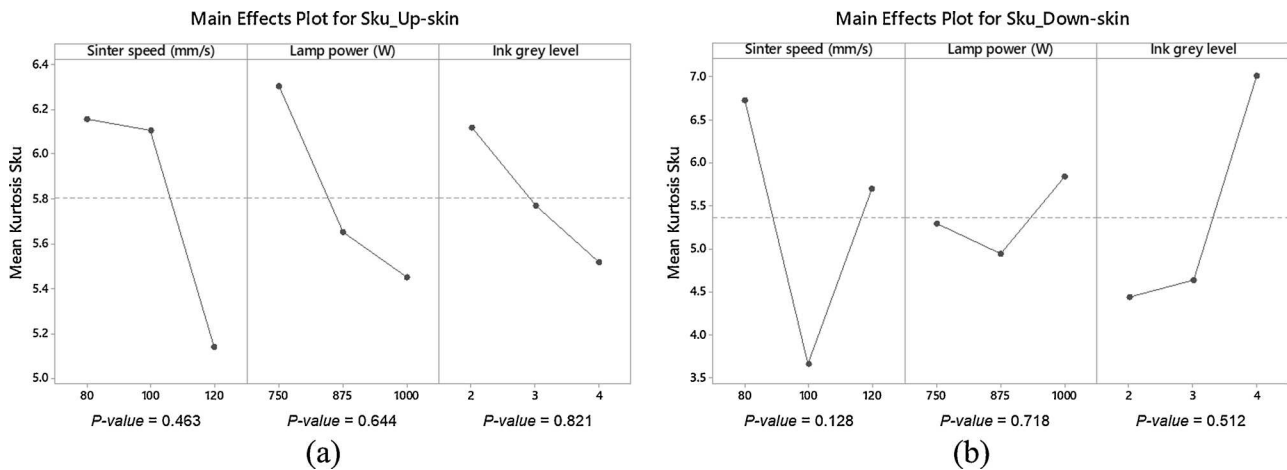


Fig. 13. Main effects plots for kurtosis (*Sk_u*) in relation to the HSS process parameters.

top surface profiles of sets 3 and 5 are shown in Fig. 17, demonstrating that a lower input energy directly leads to a rougher surface.

However, certain downsides of using excess energy input were also reported in other research [10,74]. One of the major drawbacks is that the surrounding powder that is in close vicinity to the fused contours of the part can undesirably coalesce and stick onto the surface. The formation of clusters of excess particles that adhere to the surface leads to increased surface roughness [75]. The excess heat can potentially be more detrimental to side surface quality. The side surfaces were found to be of consistently higher *S_a*, *S_q* and *S_v* values than those of up- and down-skins, as shown in Fig. 5–7. This is due to the nature of the HSS process i.e. the layer-by-layer manner. The top and bottom surfaces are formed during a single stroke of the lamp followed by a rapid solidification on a single layer. However, by contrast, side surfaces are formed as a result of multiple layers joining together in consecutive sintering and solidification, leading to an increased surface roughness. In addition, excess powders that stick on every layer of the side surface further diminishes the surface quality. This is likely to be the reason that the medium lamp power (i.e. 875 W) led to the lowest *S_a* and *S_v* in Figs. 10c and 11c.

Having said that, it is worth noting that, for processes such as LS or SLM where a laser beam provides intensive energy to the area of interest to melt particles, overly high energy can easily cause over-melting of powders. In case of LS, polymer pyrolysis occurs, which consequently creates a porous structure [76]. In case of SLM, powder evaporation takes place and defects such as keyholes form, which eventually affect surface roughness and porosity in a negative way [57,74]. Whereas, in HSS, the infrared lamp is used as the energy source that irradiates the entire powder bed as it moves across, shown

in Fig. 1 and Fig. 2. While the area that is covered by ink absorbs significantly more energy supplied from the lamp, a proportion of the energy is also absorbed by the un-printed powder. Above a certain level, this leads to unwanted ‘hardening’ of this powder, preventing reliable part removal without damage. This restricts the possibility to further increase energy input into the parts themselves whilst still being able to remove them successfully. In other words, it is less likely that excess energy can be introduced into the powder bed without causing any print failure, and hence there is potentially less negative impact of excess energy input on surface roughness in HSS.

With respect to porosity and mechanical properties, as presented above, a higher amount of energy input enables a more complete fusion of powder particles, and hence a reduced porosity. The relationship between porosity and mechanical properties of HSS parts is plotted in Fig. 14 as well as Fig. 18 below, demonstrating a strong correlation. Porosity is known to influence mechanical properties and it was found that cracks tended to initiate from pores by unfused powder particles [77,78]. Increased energy input improves fusion of powder particles, allowing a more complete liquid phase sintering and/or partial melting, even full melting in some circumstances to be achieved [69], and thus significantly less number of lack of fusion pores and better resulting mechanical properties. Based on the above, the link between surface roughness, porosity and UTS is illustrated in Fig. 19. A greater amount of energy input results in lower surface roughness and porosity, and better resulting mechanical properties. Additionally, it should be noted that particle packing density on the powder bed may also affect porosity and surface quality, which will be elaborated in Section 4.2.2.

In comparison to *S_a*, *S_q* and *S_v* that can be directly indicated by the porosity level, skewness *S_{sk}* and kurtosis *Sk_u* were not found to be in

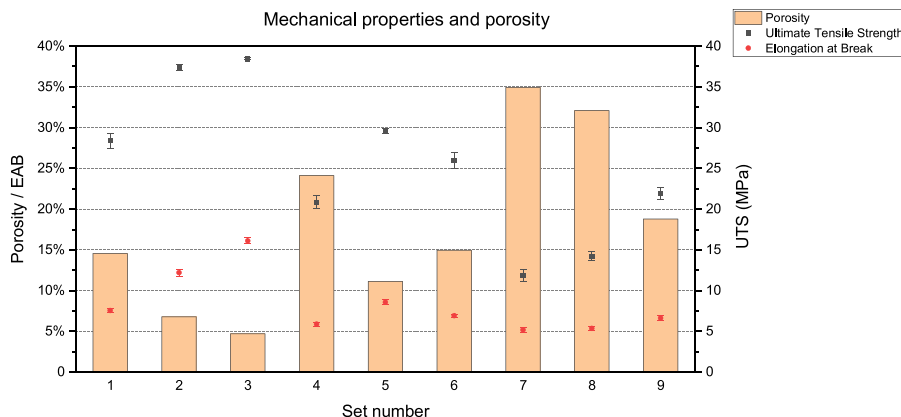


Fig. 14. Porosity and the resulting Ultimate Tensile Strength and Elongation at Break across the nine sample sets.

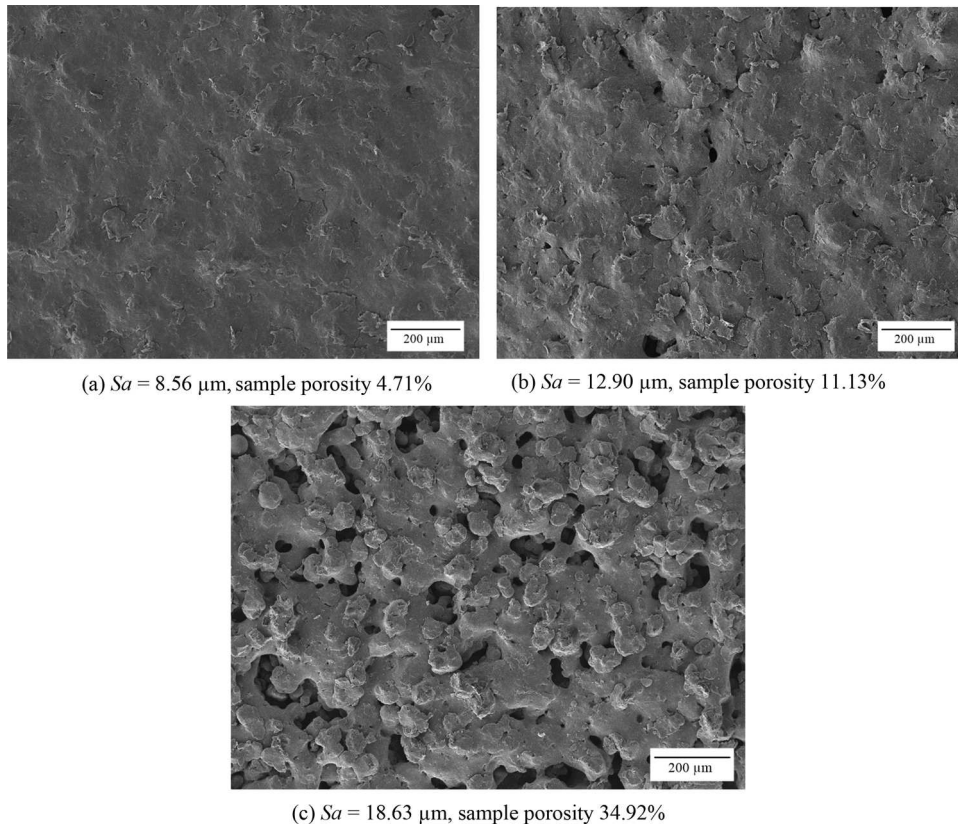


Fig. 15. SEM micrographs of the up-skins of the samples in sets 3, 5 and 7, which correspond to a low, medium and high level of energy input. It shows the amount of energy input influenced the sample porosity levels as well as surface topographies.

the same relationship with porosity. This is due to the nature of Ssk and Sku parameters, which are generally more suited for differentiating up- and down-skins of the samples that are produced in different build orientations [13,35], as well as for characterising surfaces of SLM/EBM parts where intensive energy (i.e. laser/electron beam) interacts with powder, creating a number of weld tracks i.e. rippling effect [9]. However, all samples were built horizontally in this study, and the lamp enabled particle coalescence in one lamp stroke rather than multiple scans as in SLM. Having said that, certain trends can still be observed. As the lamp passes over the powder bed, insufficient energy input leads to lack of fusion pores. Ssk value was lower than zero for the majority of the up-skins of the samples shown in Fig. 8, except for set 3 (the highest density), indicating that up-skins primarily consisted of valleys largely due to the presence of open pores on the surface. This supports the finding that energy input is one of the fundamental reasons that causes varying surface topographies. When inputting a higher amount of energy (by using a lower sinter speed, a higher lamp power and/or a higher ink grey level, as shown in Fig. 12a), there were less number of open pores/valleys and Ssk (negative value) increased towards zero. Similarly, for down-skin Ssk , increasing sinter speed and decreasing

lamp power effectively reduced input energy, leading to a decreased negative Ssk value, namely, more open pores on the surface (Fig. 12b).

Kurtosis Sku characterises the sharpness of a surface and the nominal cut-off value is 3. All surfaces measured were found to have a Sku value greater than 3, indicating that the majority of peaks and valleys was sharp. Despite all that, both up- and down-skin Sku values reduced towards 3 as the lamp power increased, as presented in Fig. 13. It demonstrates that higher lamp powers enabled a more complete fusion of particles, producing a smoother surface i.e. peaks and valleys became less sharp. This is also consistent with the surface profiles plotted in Fig. 17 where peaks and valleys on set 3 are smoother than those on set 5. Furthermore, it should be noted that both up- and down-skin Ssk and Sku involve a series of complications, particularly for down-skin, as it undergoes under a number of heating cycles when the layers above it are melted and solidifies. Therefore, Ssk and Sku are more related to sub-surface porosity, which will be discussed in Section 4.4.

4.2.2. Powder rheological characteristics

An important aspect that affects surface topography is powder rheological characteristics. Surface topography of as-build parts is

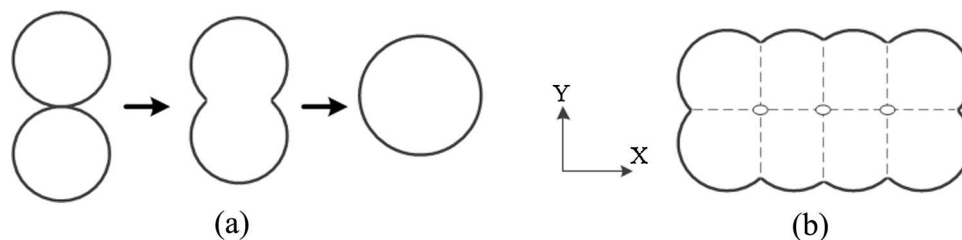


Fig. 16. Schematic representation of the sintering of particles based on the Frenkel-Eshelby model [66–68]: (a) sintering sequence for two spherical particles and (b) sintering of multiple particles, adapted from [64,69].

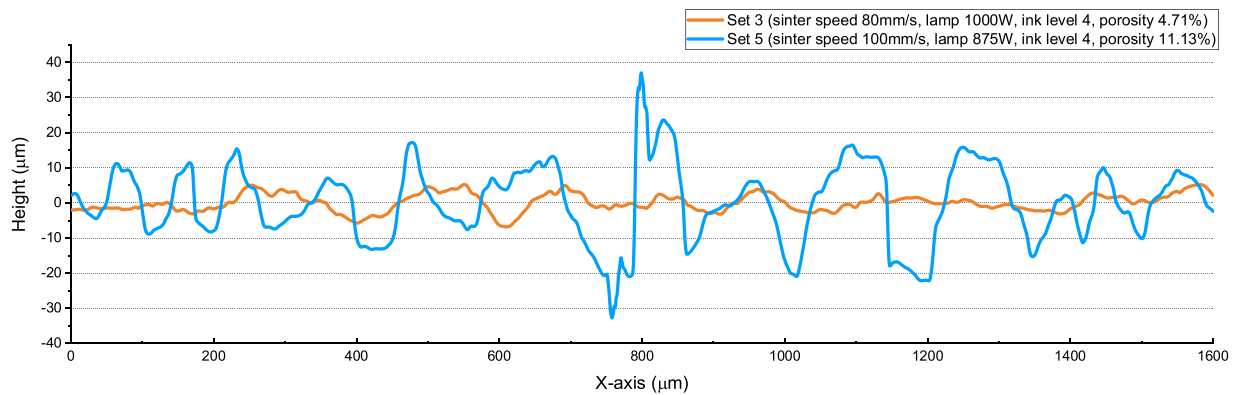


Fig. 17. Comparison of the surface profiles of the samples in sets 3 and 5.

associated with thermal phenomena and the resulting powder flow properties [79]. It is well known that powder physical properties (e.g. particle shape, size, stiffness and surface texture) influence the powder flowability, hence the packing/compaction density of the powder bed [80]. This will eventually affect the surface roughness of the as-built part [81–83], as well as other properties including porosity and tensile strength [56,84]. Basic flowability energy (BFE), which quantifies the energy required to displace a powder during non-gravitational forced flow, and specific energy (SE), which measures how easily a powder flows in an unconstrained environment, are the two indicators for powder permeability that is influential to the thermal environment/energy input during the HSS process. Reduced permeability indicated by an increased SE has been found to link to poor layer uniformity [85]. Low permeability causes air to be retained in the bulk while dispensing a new layer of powder, leading to inconsistency in powder spreading, as a result, imperfections in the sintered part surface.

An SEM image of the PA2200 virgin powders used in this study is shown in Fig. 20. It can be identified that particles are of different sizes and irregular shapes. This will lead to an increased amount of BFE (increased inter-particles surface friction and cohesion forces) and consequently decreased flowability and powder packing density, compared with spherical particles. Moreover, varying particle sizes and shapes require higher aeration energy during powder spreading, in other words, increased resistance to air flow, which negatively affects the packing density [81]. While the particle size distribution is considered to be consistent in this study (all powders used were commercial virgin powders provided by EOS GmbH), the influence of varying particle sizes and shapes on powder rheological behaviours at different thermal phenomena, caused by different levels of energy input, is currently unknown, and that requires further investigation. In addition, Fig. 20 also shows there are small quantities of flow additive. It was reported by Clayton et al. [85] that adding flow additive resulted in a

higher BFE and generated a higher pressure drop (PD), enabling powders to flow easily and achieving a denser packing within the bulk. However, powder flowability with flow additive may vary significantly in different thermal environments. Again, further effort will need to be made on understanding the effect of flow additive on powder rheology at varying amount of input energy in HSS. This includes dynamic flow, aeration, permeability, compressibility and shear testing. This will identify critical parameters in relation to varying temperatures, such as aeration energy, cohesion coefficient, BFE, SE and PD, which are effective indicators to characterise powder flowability.

It is apparent that powder thermal conductivity of bulk powders directly affects energy absorption and temperature distribution of the powder bed. It is also apparent that thermal conductivity is directly influenced by the powder packing density, which highly depends on the above-mentioned powder characteristics (e.g. powder morphology). The variation of surface roughness values can be attributed to the presence of voids and partially sintered particles, as shown in Fig. 15, that is partially caused by the incompact powder bed density [56]. Therefore, it is believed that there is a link between powder rheology and surface roughness. A better rheological behaviour will result in a better flowability during powder spreading, leading to a more efficient packing and associated energy absorption. This will eventually favour the formation of parts with an increased density and improved surface roughness.

Another thing to note is that, uniformity of each layer during a build may also be influential to the surface roughness of a final part in addition to powder packing density. An uneven layer, which is largely due to insufficient energy input, may result in variations in the dynamics of powder-infrared lamp interactions and packing density for the next layer. An example of the complications caused by an uneven layer is illustrated in Fig. 21. Large and deep voids on the previous uneven layer can easily trap particles of certain sizes and shapes when spreading a

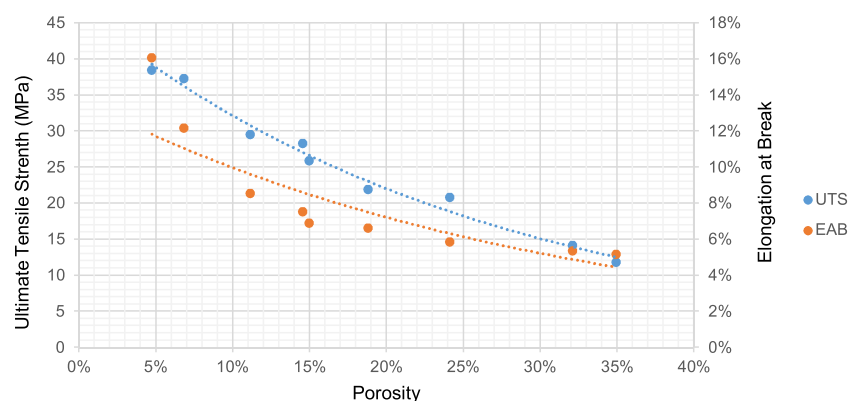


Fig. 18. Relationship between porosity and mechanical properties.

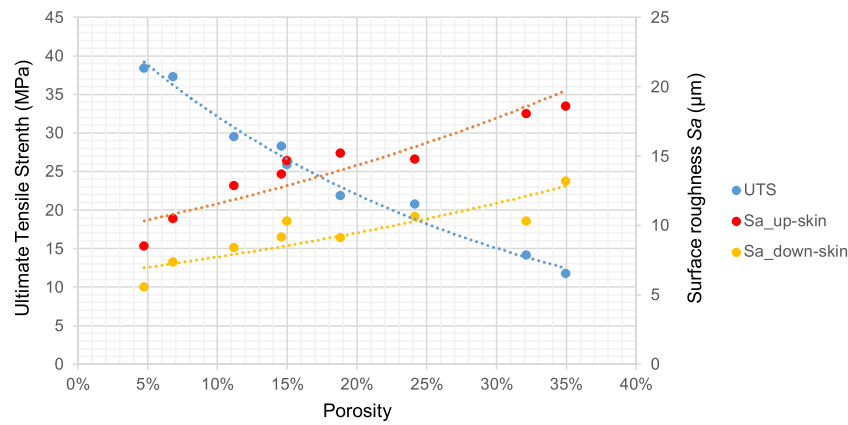


Fig. 19. Relationship between surface roughness Sa, porosity and ultimate tensile strength.

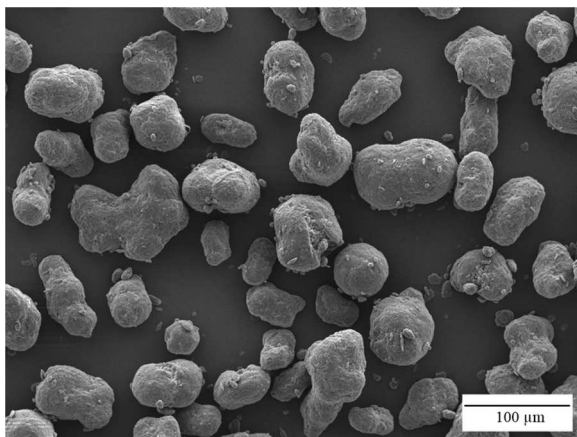


Fig. 20. Micrograph of the virgin PA2200 powders used in this study.

new layer of powder. This introduces additional complexity in powder rheological behaviour and thus potentially negatively affects powder packing density for the next layer. Less amount of energy input, a more uneven layer (e.g. the set 5 surface shown in Fig. 17), and as a result, more complex powder rheology issues and reduced surface roughness.

In addition, it is worth noting that materials generally exhibit different rheological behaviours in solid and liquid states. Even in the same powder packing density condition, varying amounts of energy input can result in different thermal phenomena. This will affect the rheological characteristics of material being melted, causing variations

in surface roughness. Temperature distribution is a direct result of energy density that is the combinational effect of lamp power, sinter speed and ink grey level. When the interface of the powders is subject to localised heat, surface tension reduces. This interface between the hot (current layer, liquid/semi-liquid state) and cool (previous layers, solid state) area induces a gradient of surface tension that rapidly propagates towards the surrounding area. An excess amount of input energy leads to a high gradient of surface tension, causing a slight motion of the liquid and thus forming irregularity on the surface during rapid solidification [57]. As a result, the surface roughness is negatively affected. However, a thorough understanding on rheological behaviours is yet to be acquired, especially for interactions of surface energy, capillary force, intermolecular forces and work adhesion involved in the HSS process.

4.3. Measurement limitations and discrepancies

4.3.1. Re-entrant features

AM surfaces are known with re-entrant features which place a significant challenge for metrology [9,25]. The measurement technique used in this study is FV, which relies on the reflection of the light from the surface. However, highly porous samples (e.g. sets 4, 7, 8 & 9) usually have re-entrant features on the side surfaces, which increases measurement discrepancies, especially in measuring S_v , S_{sk} and S_{ku} . Some typical re-entrant features are shown in Fig. 22 that were not detectable in the FV measurements due to its line-of-sight restriction. Therefore, S_{sk} and S_{ku} for side surfaces were not analysed in the paper. The implication of S_v on mechanical properties is also inconclusive,

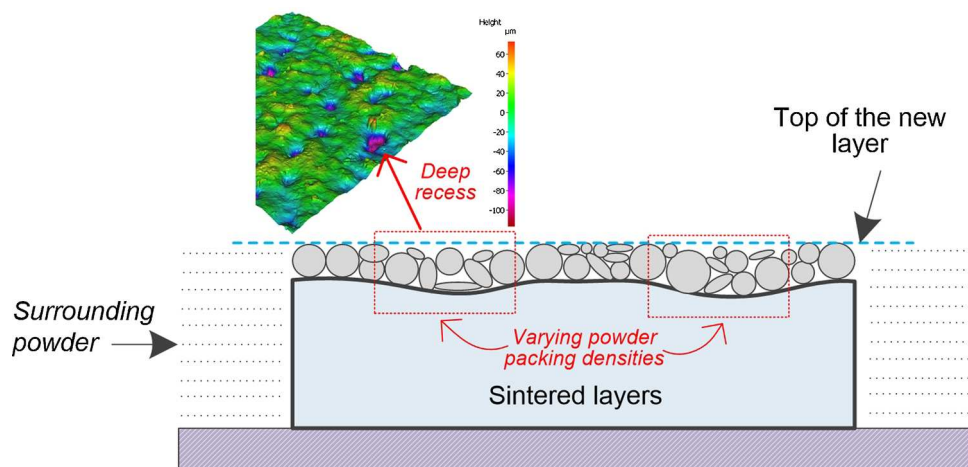


Fig. 21. Demonstration of the impact of layer uniformity on powder rheological behaviour and powder bed packing density.

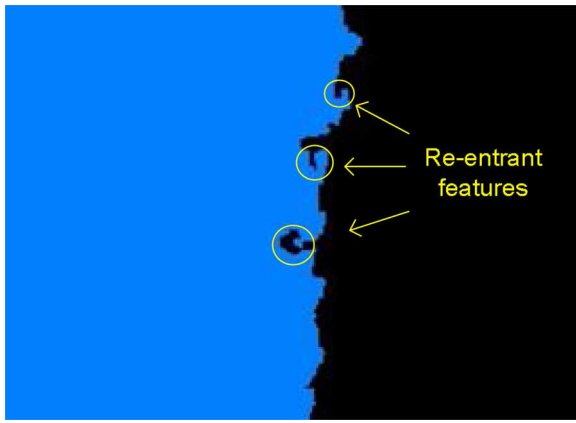


Fig. 22. Re-entrant features on the side surface of the set 4 sample, imaged and processed by XCT (sample is in blue and air is in black).

despite the fact that S_v appears to correlate with porosity shown in Fig. 7. XCT is a promising technique to acquire a more precise surface topography as X-rays can travel through re-entrant features [6]. However, XCT is also constrained by other factors such as voxel size, scan time and surface determination etc. It is possible, though time-consuming, to XCT scan (in-situ) the entire gauge length of the tensile bar under tension to identify the maximum valley depth and the position, and to match it with the location where the crack started to initiate.

4.3.2. Sphere-like protrusions and recesses

Surface topography in PBF AM is a result of fusion and subsequent solidification of powder particles. HSS is different from LS, SLM and EBM where a laser or electron beam is used to scan the surface of the part resulting in surface topography being typically dominated by weld tracks. However, certain singularities were observed on HSS part surfaces, typically consisting of sphere-like protrusions and deep recesses.

Fig. 23 compares the surface topographies between sphere-like protrusions (Fig. 23a) and a more 'normal' down-skin surface (Fig. 23b). It is apparent that the dense population of sphere-like protrusions significantly affected the measured surface texture parameters. Protrusions are formed either from unsintered or partially-sintered powder particles that stuck on the surface, particularly due to insufficient heat. Therefore, they can appear alone and in clusters as shown in Fig. 23a. It was further noticed that sphere-like protrusions were usually found at edges where two surfaces of the part intersect, in particular in sets 4, 7 & 8 where the amount of energy input was low. The reason that caused the inhabitancy of protrusions at edges is unknown in this study, which might be linked with the presence of slight thermal gradients at surface edges. In order to obtain consistent and less discrepant results, sphere-like protrusion were excluded to the authors'

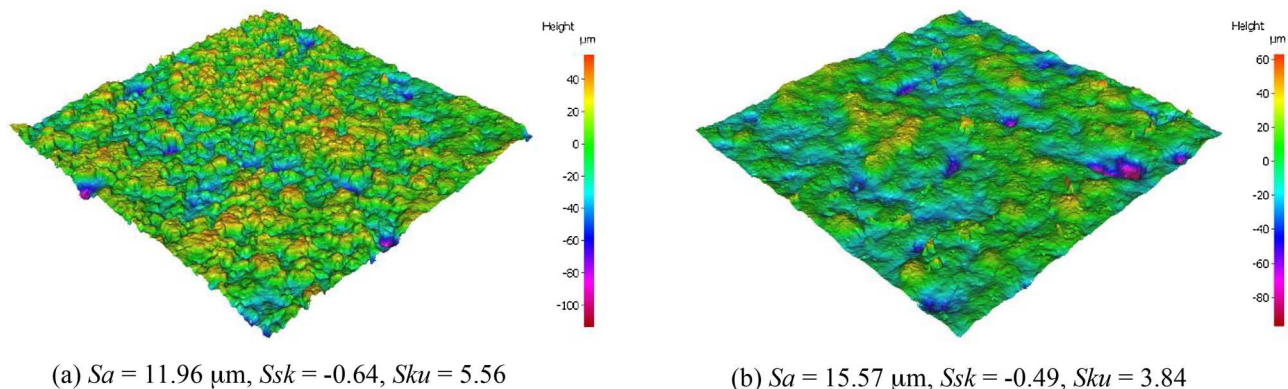


Fig. 23. The down-skin surfaces ($2 \times 2 \text{ mm}^2$) of the set 8 sample. (a) shows sphere-like protrusions on the surface and (b) shows a more 'normal' down-skin surface.

best knowledge by visual examination of the scanned surfaces.

Deep recesses are another typical feature observed. Increased number of recesses was found on surfaces of the samples with a higher porosity level e.g. set 7 in Fig. 15c. It was believed that deep recesses were open pores at the micro level, and they were formed as a result of lack of fusion. The surfaces of a part are in contact with surrounding unsintered powders that are inherently of low temperature. This leads to more open pores to form, eventually becoming deep recesses, some of which develop into re-entrant recesses that have a large and negative impact on surface topography as well as measurement reliability. This is also potentially the reason for side surface's S_a , S_q and S_v that were found not to closely correlate with the process parameters in Figs. 10 and 11.

4.4. Sub-surface porosity

S_a , S_q and S_v for up- and down-skins have shown a strong correlation with energy input and the resulting porosity, as demonstrated in a number of graphs in Figs. 5–7, 10, 11 & 19. They increased or decreased in a good consistency with the changes in the HSS process parameters and porosity levels. However, no clear trend was found for skewness S_{sk} and kurtosis S_{ku} in relation to porosity in Fig. 8 and Fig. 9. They are the parameters characterising the distribution and sharpness of peaks and valleys on the surface, and thus are more susceptible not only to process parameters but also to other factors such as sphere-like protrusions.

However, the overall porosity of the entire sample is most unlikely to be adequate as an independent factor to link with S_{sk} and S_{ku} . It is seen that, for samples with a high level of overall porosity (e.g. set 4 shown in Table 3), there is a visible difference between the sub-surface porosities of up- and down-skins. Hence, in comparison to the overall porosity, sub-surface porosity potentially has a greater impact on S_{sk} and S_{ku} values, and some observations are discussed below.

- Fig. 8 shows the variation of up-skin S_{sk} is not consistent with that of down-skin S_{sk} . Similarly, the variation of up-skin S_{ku} is not consistent with that of down-skin S_{ku} either, as shown in Fig. 9.
- Neither up- nor down-skin S_{sk} and S_{ku} was found to be in a good relation to the overall porosity of the entire sample in Figs. 8 and 9.
- Most of the up-skin S_{sk} and S_{ku} values were largely different to the down-skin S_{sk} and S_{ku} values, respectively, in Figs. 8 and 9. By visual examination of the XCT tomography images in Table 3, it was found that the up-skin sub-surface showed a more porous structure than the down-skin sub-surface. Some examples are sets 4, 5, 6 and 9.
- Volume rendering of the sub-surface porosities of the up- and down-skins of the set 6 sample is shown in Fig. 24. A noticeable difference between the two sub-surface porosities can be identified, which led to the difference in up- and down-skin S_{sk} and S_{ku} values.

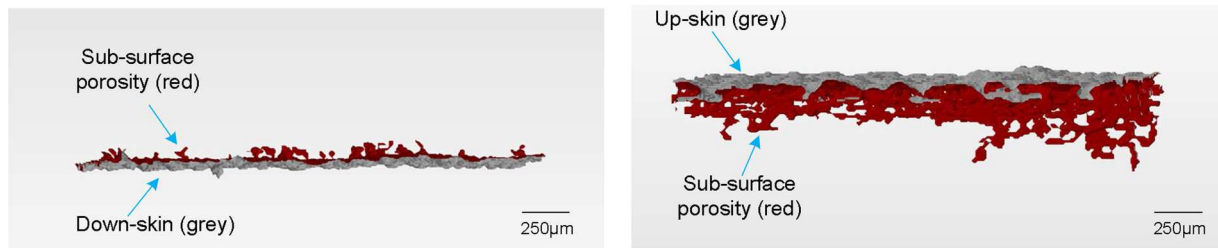


Fig. 24. Volume rendering of the sub-surface porosity (in red) of the up- and down-skins of the set 6 sample, showing a visible difference.

- For sets 4, 5, 6 and 9, down-skin Sku had similar values, shown in Fig. 9. Down-skin Ssk was also found to have similar values for these sets. Given that the down-skin of these sets showed similar sub-surface porosities in Table 3, this suggests Ssk and Sku are more closely related to sub-surface porosity as opposed to the overall porosity of the sample.
- All up-skin Ssk had a negative value (except for set 3), and was lower than the corresponding down-skin Ssk value, as shown in Fig. 8, suggesting that up-skins were predominated by valleys due to the existence of micro open pores. As presented above, up-skin sub-surface was generally more porous than down-skin sub-surface. This was because down-skin was subject to a number of heating cycles when the subsequent layers were melted by the lamp. This resulted in additional thermal energy dissipating into the down-skin and the adjacent layers, enhancing the fusion of powder particles. Whereas, the up-skin (the top layer of the part) was subject to a gradual cooling process as soon as it was printed, leading to the sub-surface being more porous.

Although Ssk/Sku can potentially be linked with sub-surface porosity, further work is required to investigate the correlation between surface topography and sub-surface porosity.

4.5. Areal surface texture and mechanical properties

Despite correlations between surface texture parameters (Sa , Sq and Sv) and porosity, as well as porosity and mechanical properties having been established, the direct effect of certain surface texture features on the mechanical properties cannot be quantified. The mechanical properties are the consequence of a series of interactions between thermal energy, bonding between layers and consolidated part as well as surrounding un-sintered powders. Measuring Sa , Sq and Sv may provide an indication of possible mechanical properties directly, i.e. an increasing Sa , Sq and Sv indicates the part having a reduced UTS and EAB in general. Nevertheless, the failure of a tensile bar in tensile testing is never simply caused by the maximum valley depth Sv alone, or the highest Sa , as discussed in Sections 4.2 and 4.3.1.

A failure takes place in the location where is likely caused by a combined influence of a surface notch (e.g. high value of Sv and $Sku > 3$ sharp valleys) and a cluster of sub-surface pores making the structure inherently weak [4]. A typical example can be found in Fig. 25a and b where the sample in set 7 shows a highly porous side surface adhered with partially sintered powder particles (protrusions). Large and deep recesses were present, that were considered as defects for mechanical properties. A fracture surface is shown in Fig. 25c consisting of existing internal pores prior to tensile testing, which were also detrimental to the mechanical strength, resulting in the reduced capability to withstand the tensile load.

5. Concluding remarks

This study investigated the areal surface texture of High Speed Sintered parts and correlated it with the process parameters (sinter speed, lamp power and ink grey level), porosity and mechanical

properties. The FV surface measurement technique was used to systematically examine the surface topography of up-, down-skins and side surfaces, and the porosity was quantified by using XCT and MIP techniques. Based on the results presented and discussed in the preceding sections, the following conclusions are derived.

Surface arithmetic mean height (Sa), root-mean-square height (Sq) and maximum valley depth (Sv) have shown to be strongly correlated with the porosity levels. A higher value of Sa , Sq or Sv indicates a high level of porosity. Reduced porosity also reflects on a decrease in Sa , Sq and Sv , leading to a smoother surface. In terms of process parameters, a clear trend was identified for Sa , Sq and Sv for up and down-skins. They increased as the sinter speed increased, and they decreased as the lamp power and ink grey level increased. This suggests that a higher level of energy input can effectively result in improved surface roughness. Up- and down-skin kurtosis Sku was found to be greater than 3, indicating that the surface is characterised by spiked surface roughness with peaks and valleys having relatively sharp edges with small edge radius.

Porosity was further found to be closely correlated with UTS and EAB. The fundamental reason is the energy input. A higher degree of fusion of powder particles was caused by a greater amount of energy, resulting in formation of parts with reduced porosity and improved mechanical properties. A sufficiently high amount of energy input enables powder particle to fuse and consolidate, leading to a more uniform and smoother surface. Surface texture parameters Sa , Sq and Sv were found to be good indicators for porosity, UTS and EAB. However, it should be noted that mechanical properties are the result of a series of complex interactions between thermal energy, particle coalescence, layer bonding and surrounding powders. Thus, the mechanical properties of a finished part are the combinational influences of overall porosity, sub-surface porosity, material properties and surface topography. Future work will focus on characterising and correlating sub-surface porosity with surface topography. The influence of rheological behaviours of powders as well as melted material in different thermal phenomena on surface roughness of the finished part will also be investigated, which will provide a thorough understanding of the formation of surface topography.

Author statement

This is to declare that the work presented in the paper is original and is not being considered/submitted elsewhere.

Declaration of Competing Interest

The authors declare that they have no known competing financial interests or personal relationships that could have appeared to influence the work reported in this paper.

Acknowledgements

This research is funded by the UK Engineering and Physical Sciences Research Council, grant number EP/P006566/1. Thanks also go to Dr Julia Behnsen from the Henry Moseley X-ray Imaging Facility at the University of Manchester for her assistance in XCT scans, and Mr Kurt

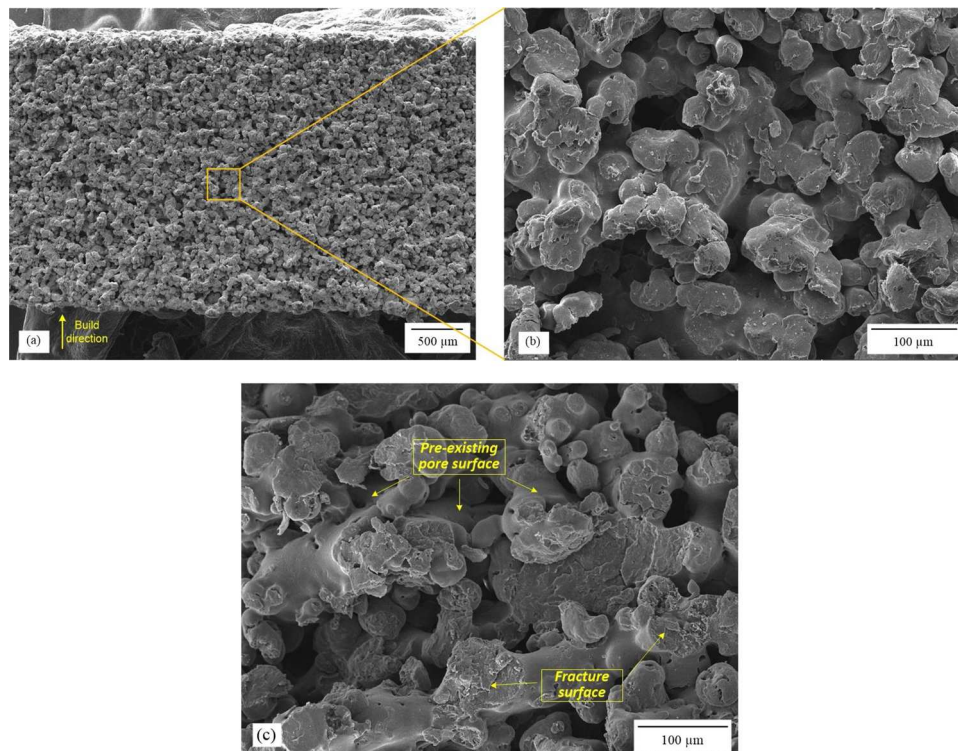


Fig. 25. SEM micrographs: (a) and (b) the side surface topography, and (c) fracture surface of the sample in set 7.

Bonsler at the University of Sheffield for his assistance in HSS processing.

References

- [1] T.D. Ngo, A. Kashani, G. Imbalzano, K.T.Q. Nguyen, D. Hui, Additive manufacturing (3D printing): a review of materials, methods, applications and challenges, *Compos. Part B Eng.* 143 (2018) 172–196, <https://doi.org/10.1016/j.compositesb.2018.02.012>.
- [2] S.A.M. Tofail, E.P. Koumoulos, A. Bandyopadhyay, S. Bose, L. O'Donoghue, C. Charitidis, Additive manufacturing: scientific and technological challenges, market uptake and opportunities, *Mater. Today* 21 (2018) 22–37, <https://doi.org/10.1016/j.mattod.2017.07.001>.
- [3] A. Townsend, N. Senin, L. Blunt, R.K. Leach, J.S. Taylor, Surface texture metrology for metal additive manufacturing: a review, *Precis. Eng.* 46 (2016) 34–47, <https://doi.org/10.1016/j.precisioneng.2016.06.001>.
- [4] J. Gockel, L. Sheridan, B. Koerper, B. Whip, The influence of additive manufacturing processing parameters on surface roughness and fatigue life, *Int. J. Fatigue* 124 (2019) 380–388, <https://doi.org/10.1016/j.ijfatigue.2019.03.025>.
- [5] T. Grimm, G. Wiora, G. Witt, Quality control of laser-beam-melted parts by a correlation between their mechanical properties and a three-dimensional surface analysis, *JOM* 69 (2017) 544–550, <https://doi.org/10.1007/s11837-016-2190-9>.
- [6] R.K. Leach, D. Bourell, S. Carmignato, A. Donmez, N. Senin, W. Dewulf, Geometrical metrology for metal additive manufacturing, *CIRP Ann. Manuf. Technol.* 68 (2019) 677–700, <https://doi.org/10.1016/j.cirp.2019.05.004>.
- [7] A. Charles, A. Elkaseer, L. Thijs, V. Hagenmeyer, S. Scholz, Effect of process parameters on the generated surface roughness of down-facing surfaces in selective laser melting, *Appl. Sci.* 9 (2019) 1256, <https://doi.org/10.3390/app9061256>.
- [8] A. Charles, A. Elkaseer, T. Mueller, L. Thijs, V. Hagenmeyer, S. Scholz, Effect of process parameters on dimensional accuracy of down-facing surfaces in selective laser melting of Ti6Al4V, *ASPE and Euspen Summer Topical Meeting - Advancing Precision in Additive Manufacturing*, Berkeley, California, USA, 2018, pp. 83–88.
- [9] B. Whip, L. Sheridan, J. Gockel, The effect of primary processing parameters on surface roughness in laser powder bed additive manufacturing, *Int. J. Adv. Manuf. Technol.* 103 (2019) 4411–4422, <https://doi.org/10.1007/s00170-019-03716-z>.
- [10] I. Koutiri, E. Pessard, P. Peyre, O. Amlou, T. De Terris, Influence of SLM process parameters on the surface finish, porosity rate and fatigue behavior of as-built Inconel 625 parts, *J. Mater. Process. Technol.* 255 (2018) 536–546, <https://doi.org/10.1016/j.jmatprotec.2017.12.043>.
- [11] F. Calignano, D. Manfredi, E.P. Ambrosio, L. Iuliano, P. Fino, Influence of process parameters on surface roughness of aluminum parts produced by DMLS, *Int. J. Adv. Manuf. Technol.* 67 (2013) 2743–2751, <https://doi.org/10.1007/s00170-012-4688-9>.
- [12] J.C. Fox, S.P. Moylan, B.M. Lane, Effect of process parameters on the surface roughness of overhanging structures in laser powder bed fusion additive manufacturing, *Procedia Cirp* 45 (2016) 131–134, <https://doi.org/10.1016/j.procir.2016.02.347>.
- [13] A.T. Sidambe, Three dimensional surface topography characterization of the electron beam melted Ti6Al4V, *Met. Powder Rep.* 72 (2017) 200–205, <https://doi.org/10.1016/j.mprp.2017.02.003>.
- [14] Y. Tian, D. Tomus, P. Rometsch, X. Wu, Influences of processing parameters on surface roughness of Hastelloy X produced by selective laser melting, *Addit. Manuf.* 13 (2017) 103–112, <https://doi.org/10.1016/j.addma.2016.10.010>.
- [15] G. Strano, L. Hao, R.M. Everson, K.E. Evans, Surface roughness analysis, modelling and prediction in selective laser melting, *J. Mater. Process. Technol.* 213 (2013) 589–597, <https://doi.org/10.1016/j.jmatprotec.2012.11.011>.
- [16] A. Thompson, S. Tammam-Williams, N. Senin, I. Todd, R. Leach, *Correlating volume and surface features in additively manufactured metal parts*, *ASPE and Euspen Summer Topical Meeting in Advancing Precision in Additive Manufacturing*, Berkeley, California, USA, 2018, pp. 116–120.
- [17] J. Han, Y. Ge, Y. Mao, M. Wu, A study on the surface quality of the 3D printed parts caused by the scanning strategy, *Rapid Prototyp. J.* 25 (2019) 247–254, <https://doi.org/10.1108/RPJ-06-2017-0125>.
- [18] N.K. Mavoori, S. Vekatesh, M.H. M, Investigation on surface roughness of sintered PA2200 prototypes using Taguchi method, *Rapid Prototyp. J.* 25 (2019) 454–461, <https://doi.org/10.1108/RPJ-10-2017-0201>.
- [19] A. Sachdeva, S. Singh, V.S. Sharma, Investigating surface roughness of parts produced by SLS process, *Int. J. Adv. Manuf. Technol.* 64 (2013) 1505–1516, <https://doi.org/10.1007/s00170-012-4118-z>.
- [20] S. Negi, S. Dhiman, R.K. Sharma, Investigating the surface roughness of SLS fabricated glass-filled polyamide parts using response surface methodology, *Arab. J. Sci. Eng.* 39 (2014) 9161–9179, <https://doi.org/10.1007/s13369-014-1434-7>.
- [21] B. Van Hooreweder, D. Moens, R. Boonen, J.-P. Kruth, P. Sas, On the difference in material structure and fatigue properties of nylon specimens produced by injection molding and selective laser sintering, *Polym. Test.* 32 (2013) 972–981, <https://doi.org/10.1016/j.polymertesting.2013.04.014>.
- [22] G. Strano, L. Hao, R.M. Everson, K.E. Evans, Multi-objective optimization of selective laser sintering processes for surface quality and energy saving, *Proc. Inst. Mech. Eng. Part B J. Eng. Manuf.* 225 (2011) 1673–1682, <https://doi.org/10.1177/0954405411402925>.
- [23] L. Pagani, A. Townsend, W. Zeng, S. Lou, L. Blunt, X.Q. Jiang, P.J. Scott, Towards a new definition of areal surface texture parameters on freeform surface: Re-entrant features and functional parameters, *Measurement* 141 (2019) 442–459, <https://doi.org/10.1016/j.measurement.2019.04.027>.
- [24] A. du Plessis, S.G. le Roux, Standardized X-ray tomography testing of additively manufactured parts: a round robin test, *Addit. Manuf.* 24 (2018) 125–136, <https://doi.org/10.1016/j.addma.2018.09.014>.
- [25] F. Zanini, L. Pagani, E. Savio, S. Carmignato, Characterisation of Additively Manufactured Metal Surfaces by Means of X-ray Computed Tomography and Generalised Surface Texture Parameters, *CIRP Annals*, 2019, <https://doi.org/10.1016/j.cirp.2019.04.074>.
- [26] S. Lou, X. Jiang, W. Sun, W. Zeng, L. Pagani, P.J. Scott, Characterisation methods

- for powder bed fusion processed surface topography, *Precis. Eng.* 57 (2019) 1–15, <https://doi.org/10.1016/j.precisioneng.2018.09.007>.
- [27] C.G. Klingaa, M.K. Bjerre, S. Baier, L. De Chiffre, S. Mohanty, J.H. Hattel, Roughness investigation of SLM manufactured conformal cooling channels using X-ray computed tomography, 9th Conference on Industrial Computed Tomography, Padova, Italy, 2019, pp. 1–10.
- [28] M. Vetterli, M. Schmid, W. Knapp, K. Wegener, New horizons in selective laser sintering surface roughness characterization, *Surf. Topogr. Metrol. Prop.* 5 (2017) 45007, <https://doi.org/10.1088/2051-672x/aa88ee>.
- [29] M. Launhardt, A. Wörz, A. Loderer, T. Laumer, D. Drummer, T. Hausotte, M. Schmidt, Detecting surface roughness on SLS parts with various measuring techniques, *Polym. Test.* 53 (2016) 217–226, <https://doi.org/10.1016/j.polymertesting.2016.05.022>.
- [30] A. Thompson, N. Senin, I. Maskery, L. Körner, S. Lawes, R. Leach, Internal surface measurement of metal powder bed fusion parts, *Addit. Manuf.* 20 (2018) 126–133, <https://doi.org/10.1016/j.addma.2018.01.003>.
- [31] A. Townsend, L. Pagani, P. Scott, L. Blunt, Areal surface texture data extraction from X-ray computed tomography reconstructions of metal additively manufactured parts, *Precis. Eng.* 48 (2017) 254–264, <https://doi.org/10.1016/j.precisioneng.2016.12.008>.
- [32] G. Kerckhofs, G. Pyka, M. Moesen, S. Van Bael, J. Schrooten, M. Wevers, High-resolution microfocus X-ray computed tomography for 3D surface roughness measurements of additive manufactured porous materials, *Adv. Eng. Mater.* 15 (2013) 153–158.
- [33] A. Thompson, N. Senin, C. Giusca, R. Leach, Topography of selectively laser melted surfaces: a comparison of different measurement methods, *CIRP Ann. Manuf. Technol.* 66 (2017) 543–546, <https://doi.org/10.1016/j.cirp.2017.04.075>.
- [34] A. Townsend, R. Racasan, R. Leach, N. Senin, A. Thompson, A. Ramsey, D. Bate, P. Woolliams, S. Brown, L. Blunt, An interlaboratory comparison of X-ray computed tomography measurement for texture and dimensional characterisation of additively manufactured parts, *Addit. Manuf.* 23 (2018) 422–432, <https://doi.org/10.1016/j.addma.2018.08.013>.
- [35] A. Triantaphyllou, C.L. Giusca, G.D. Macaulay, F. Roerig, M. Hoebel, R.K. Leach, B. Tomita, K.A. Milne, Surface texture measurement for additive manufacturing, *Surf. Topogr. Metrol. Prop.* 3 (2015) 24002, <https://doi.org/10.1088/2051-672x/3/2/024002>.
- [36] F. Cabanettes, A. Joubert, G. Chardon, V. Dumas, J. Rech, C. Grosjean, Z. Dimkovski, Topography of as built surfaces generated in metal additive manufacturing: a multi scale analysis from form to roughness, *Precis. Eng.* 52 (2018) 249–265, <https://doi.org/10.1016/j.precisioneng.2018.01.002>.
- [37] A. Ellis, C.J. Noble, N. Hopkinson, High Speed Sintering: assessing the influence of print density on microstructure and mechanical properties of nylon parts, *Addit. Manuf.* 1 (2014) 48–51.
- [38] C.E. Majewski, D. Oduye, H.R. Thomas, N. Hopkinson, Effect of infra-red power level on the sintering behaviour in the high speed sintering process, *Rapid Prototyp. J.* 14 (2008) 155–160, <https://doi.org/10.1108/13552540810878012>.
- [39] G.M. Vasquez, C.E. Majewski, B. Haworth, N. Hopkinson, A targeted material selection process for polymers in laser sintering, *Addit. Manuf.* 1–4 (2014) 127–138, <https://doi.org/10.1016/j.addma.2014.09.003>.
- [40] C.E. Majewski, B.S. Hobbs, N. Hopkinson, Effect of bed temperature and infra-red lamp power on the mechanical properties of parts produced using high-speed sintering, *Virtual Phys. Prototyp.* 2 (2007) 103–110, <https://doi.org/10.1080/17452750701520915>.
- [41] H.J. O'Connor, A.N. Dickson, D.P. Dowling, Evaluation of the mechanical performance of polymer parts fabricated using a production scale multi jet fusion printing process, *Addit. Manuf.* 22 (2018) 381–387, <https://doi.org/10.1016/j.addma.2018.05.035>.
- [42] SunChemical, *Advanced Materials: Inkjet*, (2020).
- [43] M. Ritchie, Print Quality Requirements for Single-pass Inkjet Printing – the Whole Picture, Xaar 3D Ltd., 2017 Available at:<https://www.xaar.com/media/1303/print-quality-white-paper.pdf> accessed on 30/05/2020.
- [44] U. Scipioni Bertoli, A.J. Wolfer, M.J. Matthews, J.-P.R. Delplanque, J.M. Schoenung, On the limitations of Volumetric Energy Density as a design parameter for Selective Laser Melting, *Mater. Des.* 113 (2017) 331–340, <https://doi.org/10.1016/j.matdes.2016.10.037>.
- [45] M. Guo, D. Gu, L. Xi, H. Zhang, J. Zhang, J. Yang, R. Wang, Selective laser melting additive manufacturing of pure tungsten: role of volumetric energy density on densification, microstructure and mechanical properties, *Int. J. Refract. Metals Hard Mater.* 84 (2019) 105025, <https://doi.org/10.1016/j.ijrmhm.2019.105025>.
- [46] M. Pavan, M. Faes, D. Strobbe, B. Van Hooreweder, T. Craeghs, D. Moens, W. Dewulf, On the influence of inter-layer time and energy density on selected critical-to-quality properties of PA12 parts produced via laser sintering, *Polym. Test.* 61 (2017) 386–395, <https://doi.org/10.1016/j.polymertesting.2017.05.027>.
- [47] M. Ghayoor, K. Lee, Y. He, C.-h. Chang, B.K. Paul, S. Pasebani, Selective laser melting of 304L stainless steel: role of volumetric energy density on the microstructure, texture and mechanical properties, *Addit. Manuf.* 32 (2020) 1–13, <https://doi.org/10.1016/j.addma.2019.101011>.
- [48] ASTM, D638-02a: Standard Test Method for Tensile Properties of Plastics, (2017).
- [49] A. Townsend, R. Racasan, L. Blunt, Surface-specific additive manufacturing test artefacts, *Surf. Topogr. Metrol. Prop.* 6 (2018) 24007, <https://doi.org/10.1088/2051-672x/aabcaf>.
- [50] BrukerAlicona, Alicona InfiniteFocusSL 3D Measurement System for Form & Finish, Bruker (2019).
- [51] ISO, 25178-2, Geometrical Product Specifications (GPS) - Surface Texture: Areal - Part 2: Terms, Definitions and Surface Texture Parameters, International Organization for Standardization, Geneva, Switzerland, 2012.
- [52] ISO 4287, Geometrical Product Specifications (GPS) - Surface Texture: Profile Method - Terms, Definitions and Surface Texture Parameters, International Organization of Standardization, Geneva, Switzerland, 1997.
- [53] ISO4288, Geometrical Product Specifications (GPS) — Surface Texture: Profile Method — Rules and Procedures for the Assessment of Surface Texture, International Organization of Standardization, Geneva, Switzerland, 1996.
- [54] ISO25178-3, Geometrical Product Specifications (GPS) — Surface Texture: Areal — Part 3: Specification Operators, International Organization for Standardization, Geneva, Switzerland, 2012.
- [55] L. Newton, N. Senin, C. Gomez, R. Danzl, F. Helml, L. Blunt, R. Leach, Areal topography measurement of metal additive surfaces using focus variation microscopy, *Addit. Manuf.* 25 (2019) 365–389, <https://doi.org/10.1016/j.addma.2018.11.013>.
- [56] S.E. Brika, M. Letenneur, C.A. Dion, V. Brailovski, Influence of particle morphology and size distribution on the powder flowability and laser powder bed fusion manufacturability of Ti-6Al-4V alloy, *Addit. Manuf.* 31 (2020) 100929, <https://doi.org/10.1016/j.addma.2019.100929>.
- [57] A.M. Khorasani, I. Gibson, A.R. Ghaderi, Rheological characterization of process parameters influence on surface quality of Ti-6Al-4V parts manufactured by selective laser melting, *Int. J. Adv. Manuf. Technol.* 97 (2018) 3761–3775, <https://doi.org/10.1007/s00170-018-2168-6>.
- [58] N. Otsu, A threshold selection method from gray-level histograms, *IEEE Trans. Syst. Man Cybern.* 9 (1979) 62–66.
- [59] T. Stichel, T. Frick, T. Laumer, F. Tenner, T. Hausotte, M. Merklein, M. Schmidt, A Round Robin study for selective laser sintering of polymers: back tracing of the pore morphology to the process parameters, *J. Mater. Process. Technol.* 252 (2018) 537–545, <https://doi.org/10.1016/j.jmatprot.2017.10.013>.
- [60] S. Tammam-Williams, H. Zhao, F. Léonard, F. Derguti, I. Todd, P.B. Prangnell, XCT analysis of the influence of melt strategies on defect population in Ti-6Al-4V components manufactured by Selective Electron Beam Melting, *Mater. Charact.* 102 (2015) 47–61, <https://doi.org/10.1016/j.matchar.2015.02.008>.
- [61] E. Maire, P.J. Withers, Quantitative X-ray tomography, *Int. Mater. Rev.* 59 (2014) 1–43, <https://doi.org/10.1179/1743280413Y.0000000023>.
- [62] M. Schmid, A. Amado, K. Wegener, Materials perspective of polymers for additive manufacturing with selective laser sintering, *J. Mater. Res.* 29 (2014) 1824–1832, <https://doi.org/10.1557/jmr.2014.138>.
- [63] F. Wakai, K. Katsura, S. Kanchika, Y. Shinoda, T. Akatsu, K. Shinagawa, Sintering force behind the viscous sintering of two particles, *Acta Mater.* 109 (2016) 292–299, <https://doi.org/10.1016/j.actamat.2016.03.006>.
- [64] C.T. Bellehumeur, M. Kontopoulou, J. Vlachopoulos, The role of viscoelasticity in polymer sintering, *Rheol. Acta* 37 (1998) 270–278, <https://doi.org/10.1007/s003970050114>.
- [65] S. Liu, Y.C. Shin, Additive manufacturing of Ti6Al4V alloy: a review, *Mater. Des.* 164 (2019) 107552, <https://doi.org/10.1016/j.matdes.2018.107552>.
- [66] J. Frenkel, Viscous flow of crystalline bodies under the action of surface tension, *J. Phys.* 9 (1945) 385.
- [67] J. Eshelby, Discussion of paper by AJ Shaler, Seminar on the kinetics of sintering, *Trans. AIME* 185 (1949) 806.
- [68] A.J. Shaler, Seminar on the kinetics of sintering, *JOM* 1 (1949) 796–813, <https://doi.org/10.1007/BF03398399>.
- [69] R.D. Goodridge, C.J. Tuck, R.J.M. Hague, Laser sintering of polyamides and other polymers, *Prog. Mater. Sci.* 57 (2012) 229–267, <https://doi.org/10.1016/j.pmatsci.2011.04.001>.
- [70] J. Bai, B. Zhang, J. Song, G. Bi, P. Wang, J. Wei, The effect of processing conditions on the mechanical properties of polyethylene produced by selective laser sintering, *Polym. Test.* 52 (2016) 89–93, <https://doi.org/10.1016/j.polymertesting.2016.04.004>.
- [71] L. Benedetti, B. Brulé, N. Decraemer, K.E. Evans, O. Ghita, Evaluation of particle coalescence and its implications in laser sintering, *Powder Technol.* 342 (2019) 917–928, <https://doi.org/10.1016/j.powtec.2018.10.053>.
- [72] S. Bajric, Selective Laser Sintering of PA2200: Effects of Print Parameters on Density, Accuracy, and Surface Roughness, Technical Report, Los Alamos National Laboratory (LANL), Los Alamos, United States, (2017), <https://doi.org/10.2172/1363740>.
- [73] Y. Li, D. Gu, Parametric analysis of thermal behavior during selective laser melting additive manufacturing of aluminum alloy powder, *Mater. Des.* 63 (2014) 856–867, <https://doi.org/10.1016/j.matdes.2014.07.006>.
- [74] P. Wang, W.J. Sin, M.L.S. Nai, J. Wei, Effects of processing parameters on surface roughness of additive manufactured Ti-6Al-4V via Electron beam melting, *Materials* 10 (2017) 1121, <https://doi.org/10.3390/ma10101121>.
- [75] P. Wang, J. Song, M.L.S. Nai, J. Wei, Experimental analysis of additively manufactured component and design guidelines for lightweight structures: a case study using electron beam melting, *Addit. Manuf.* 33 (2020) 101088, <https://doi.org/10.1016/j.addma.2020.101088>.
- [76] S.R. Athreya, K. Kalaitzidou, S. Das, Processing and characterization of a carbon black-filled electrically conductive Nylon-12 nanocomposite produced by selective laser sintering, *Mater. Sci. Eng. A* 527 (2010) 2637–2642, <https://doi.org/10.1016/j.msea.2009.12.028>.
- [77] M. Tang, P.C. Pistorius, J.L. Beuth, Prediction of lack-of-fusion porosity for powder bed fusion, *Addit. Manuf.* 14 (2017) 39–48, <https://doi.org/10.1016/j.addma.2016.12.001>.
- [78] B. Van Hooreweder, F. De Coninck, D. Moens, R. Boonen, P. Sas, Microstructural characterization of SLS-PA12 specimens under dynamic tension/compression excitation, *Polym. Test.* 29 (2010) 319–326, <https://doi.org/10.1016/j.polymertesting.2009.12.006>.
- [79] A. Ströndl, O. Lyckfeldt, H. Brodin, U. Ackelid, Characterization and control of powder properties for additive manufacturing, *JOM* 67 (2015) 549–554, <https://doi.org/10.1007/s11967-015-0348-8>.

- doi.org/10.1007/s11837-015-1304-0.
- [80] R. Freeman, X. Fu, Characterisation of powder bulk, dynamic flow and shear properties in relation to die filling, *Powder Metall.* 51 (2008) 196–201, <https://doi.org/10.1179/174329008X324115>.
- [81] F. Ahmed, U. Ali, D. Sarker, E. Marzbanrad, K. Choi, Y. Mahmoodkhani, E. Toyserkani, Study of powder recycling and its effect on printed parts during laser powder-bed fusion of 17-4 PH stainless steel, *J. Mater. Process. Technol.* 278 (2020) 116522, <https://doi.org/10.1016/j.jmatprotec.2019.116522>.
- [82] G. Jacob, G. Jacob, C.U. Brown, A. Donmez, The Influence of Spreading Metal Powders With Different Particle Size Distributions on the Powder Bed Density in Laser-based Powder Bed Fusion Processes, US Department of Commerce, National Institute of Standards and Technology, 2018, <https://doi.org/10.6028/NIST.AMS.100-17>.
- [83] M. Lutter-Günther, M. Bröker, T. Mayer, S. Lizak, C. Seidel, G. Reinhart, Spatter formation during laser beam melting of AlSi10Mg and effects on powder quality, *Procedia Cirp* 74 (2018) 33–38, <https://doi.org/10.1016/j.procir.2018.08.008>.
- [84] U. Ali, Y. Mahmoodkhani, S. Imani Shahabad, R. Esmailizadeh, F. Liravi, E. Sheydaeian, K.Y. Huang, E. Marzbanrad, M. Vlasea, E. Toyserkani, On the measurement of relative powder-bed compaction density in powder-bed additive manufacturing processes, *Mater. Des.* 155 (2018) 495–501, <https://doi.org/10.1016/j.matdes.2018.06.030>.
- [85] J. Clayton, D. Millington-Smith, B. Armstrong, The application of powder rheology in additive manufacturing, *JOM* 67 (2015) 544–548, <https://doi.org/10.1007/s11837-015-1293-z>.